IEEE Access
Multidisciplinary | Rapid Review | Open Access Journal

Received March 17, 2022, accepted March 27, 2022, date of publication April 5, 2022, date of current version April 18, 2022.

Digital Object Identifier 10.1109/ACCESS.2022.3165053

Research on the Residual Vibration Suppression of a Controllable Mechanism Robot

JUNJIE GONG[1,2], GANWEI CAI[1,2,3], WEI WEI[2], KECHEN ZHANG[2], AND SIXU PENG[2]

[1]School of Construction Machinery, Hunan Sany Polytechnic College, Changsha 410129, China
[2]School of Mechanical Engineering, Guangxi University, Nanning 530004, China
[3]Department of Physics and Electronic Engineering, Hechi University, Yizhou 546300, China

Corresponding author: Ganwei Cai (caiganwei@163.com)

This work was supported in part by the National Natural Science Foundation of China under Grant 51765005, in part by the Guangxi Science and Technology Major Projects under Grant Gui Ke AA19254021, and in part by the Guangxi Natural Science Foundation under Grant 2018GXNSFBA281080.

ABSTRACT The motors and reducers of traditional industrial robots are installed at the joints, which leads to large moment of inertia and difficult to effectively improve the dynamic performance of the robots. In particular, the residual vibration at the end of the robots will significantly reduce its working efficiency and fatigue life. Therefore, this paper proposes a new method to reinstall the motor and reducer near the frame, which can effectively suppress the residual vibration of the robots and simultaneously reduce the moment of inertia. Taking the series industrial robot as the research object, four types of CM robots are designed based on the theory of a multi-DOF controllable mechanism (CM). The motor and reducer of the robot are reinstalled near the frame through different branch chains, and their moments of inertia are calculated and compared. The dynamic equations of residual vibration of the four CM robots considering concentrated mass are established based on the finite element method (FEM) and Timoshenko space beam element (SBE) model, and the correctness of the equations are verified by experiments. The results show that the installation position of motor and reducer has a significant influence on the value of moment of inertia of the robot. The motor and reducer of configuration D are reinstalled near the frame by three branches, which can effectively reduce the attenuation time and amplitude of residual vibration at the end of the robot. The research provides a new idea for improving the dynamic performance of industrial robots.

INDEX TERMS Controllable mechanism robot, finite element method, moment of inertia, residual vibration suppression.

I. INTRODUCTION

Industrial robots are widely used in assembly, welding and palletizing. However, the residual vibration of industrial robots will reduce their work efficiency [1], [2] and affect the operational accuracy [3], [4]. It is therefore of great significance to suppress the residual vibration of robots. The spot welding robot [5], [6] and assembly robot [7]–[9] need to wait until the residual vibration of the working arm is reduced before they can perform their next work task [10], [11]. To enable industrial robots to complete maneuvering tasks both quickly and accurately, many researchers have conducted extensive and in-depth research on the residual vibration of robots from different aspects [12]–[14].

In the 1980s, Thompson and Liao [15], [16] studied the residual vibration of robot mechanisms with laminated composite components after their motion stopped. By optimizing the material parameters of the robot, these researchers significantly reduced the amplitude and time of residual vibration. Yavuz [17] researched a single-link flexible glass fabric reinforced epoxy-glass composite manipulator by ANSYS, and it was concluded that the residual vibration amplitudes of the flexible composite manipulator were suppressed with the proposed method by up to 99% for all velocity inputs. In engineering practice, composite components have striking advantages, such as a light weight and short attenuation time of residual vibration [18], [19]. On the one hand, the manipulator can be made of composite materials instead of metal materials to suppress the residual vibration of the manipulator, while on the other hand, we can apply damping materials to absorb the energy of residual vibration or add isolation

The associate editor coordinating the review of this manuscript and approving it for publication was Agustin Leobardo Herrera-May.

devices to quickly reduce the residual vibration time [20], [21]. For example, Biglari *et al.* [22] designed a damped link to replace a simple link and verified through experiments that the damped link has a better performance in terms of vibration suppression than the simple link. Kraus *et al.* [23] designed an active vibration absorber with three degrees of freedom. The mechanical structure of the 3-DOF absorber has been designed such that it has a multiple eigenfrequency equal to the first eigenfrequency of the robotic arm. In addition, the suppression of residual vibration by the active control method was proven to be feasible by experiments [24]. Active control includes the feedforward control method and the feedback control method. Feedforward control methods include the component synthesis method, the input shaping method [25]–[28] and the S-curve method [29]–[31]. This method does not require an additional vibration controller and is relatively convenient to implement [32]. A good effect has been achieved in the vibration suppression of industrial robots. Zhang *et al.* [33] used the component synthesis active vibration suppression method based on the zero-placement technique to construct the synthesized command in order to suppress the multi-harmonic vibration in the discrete domain at the same time. Thomsen *et al.* [34], based on fractional delay time-varying input shaping technology, proposed a vibration suppression method of multi-mode time-varying input shaping technology for industrial robot manipulators. Yoon *et al.* [35] proposed a method to reduce the residual vibration of an object moved by a robot manipulator by optimizing the acceleration/deceleration time calculated using the object's natural frequency. However, the results of vibration suppression are not ideal in the high-speed motion environment of highly coupled flexible parallel robots or space robots. Feedback control methods often require adding piezoelectric sensors and piezoelectric actuators to the structure, which can not only suppress the vibration, but also measure the vibration of a distributed parameter system [25], [36]–[40]. Zhang *et al.* [41] designed a strain and strain rate feedback (SSRF) controller and established a general motion equation, including sensors. Experiments show that the SSRF controller can effectively suppress the residual vibration of a three-degrees-of-freedom flexible parallel robot. Bai *et al.* [42] devised an adaptive fuzzy inversion control strategy for the 7- DOF dual arm control system, which can suppress the time-varying nonlinear residual vibration of the end effector caused by the inertia change of the series robot. Garcia Perez *et al.* [5] proposed a combined control scheme that divides the control system into two parts. One is sliding mode control based on cascaded PID, and the other is to attach a piezoelectric brake onto the flexible beam to realize active control of residual vibration and multiple positive positions feedback. This method requires the use of piezoelectric materials, shape memory alloys and electromagnetic rheological materials. There is no doubt that this method increases the manufacturing and maintenance cost of the robot and is not suitable for wide applications.

In summary, various methods have been proposed to suppress the residual vibration of robot manipulators, and satisfactory results have been achieved. However, these works are performed under three aspects: a lightweight design, passive control and active control. These studies do not consider the influence of the motor and reducer installed at the joint of the series robot on the residual vibration of the robot. If the motor and reducer can be installed on or near the frame, then the moment of inertia of the robot can be reduced, and its residual vibration can be suppressed. In addition, the current parallel robot is not suitable for all series robots because of its small workspace [43].

To solve these problems, this paper proposes a method to suppress the residual vibration of industrial robots from the structural design. This method does not require accurate sensors or intelligent materials. First, according to the theory of multi-DOF CM [44] and host parasitic (H-P) mechanisms [45], [46], four CM robots are designed: configuration A without a branched chain, configuration B with one branched chain, configuration C with two branched chains, and configuration D with three branched chains. In addition, the three branch chains of configuration D reinstall the motor and reducer at the robot joint near the frame. Second, the moments of inertia of the four types of robots are calculated and compared. Then, the dynamic models of the four configurations of the CM robot are established by using the FEM and Timoshenko SBE [47], and the dynamic models are fitted using the Monte Carlo method. The Newmark method is used to solve the dynamic equations. Finally, the effectiveness and reliability of the method are verified via simulation analysis and experimental results.

The remainder of this paper is structured as follows. The process of forming the CM robot from the series robot is developed in Section II. Section III gives the calculation model of the moment of inertia of the CM robot. The residual vibration models of the CM robot are established in Section IV. The moment of inertia of each CM robot is calculated and compared in Section V. In Section VI, the simulation results and experimental results are given to verify the effectiveness of adding a branch chain to suppress residual vibration. Conclusion and future work are given in Section VII.

II. CM ROBOT FORMATION PROCESS

This section analyzes the formation process of the CM mechanism and obtains four configurations for the robots. To keep the working range of the optimized robot unchanged, the angle relationship of each CM robot is given as the basis of a subsequent analysis.

A. SERIAL ROBOT

Figure 1 shows a schematic diagram of a current 4-DOF series robot mechanism, which is a series robot configuration commonly used in industrial production [9]. It can be seen from figure 1 that the mechanism belongs to

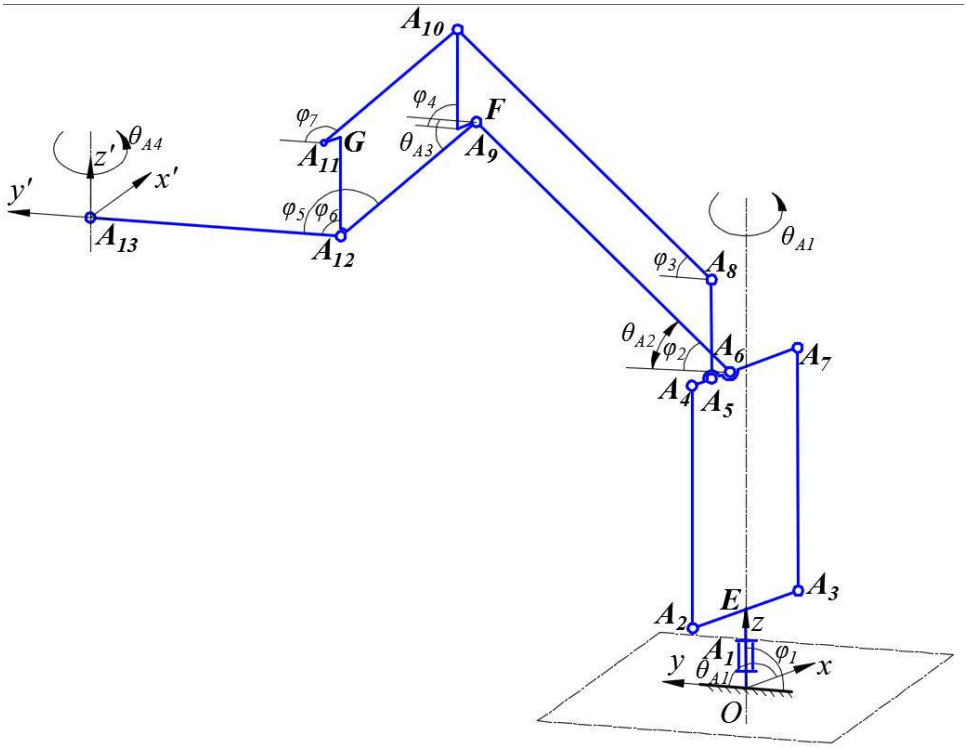

FIGURE 1. Schematic diagram of a 4-DOF series robot mechanism.

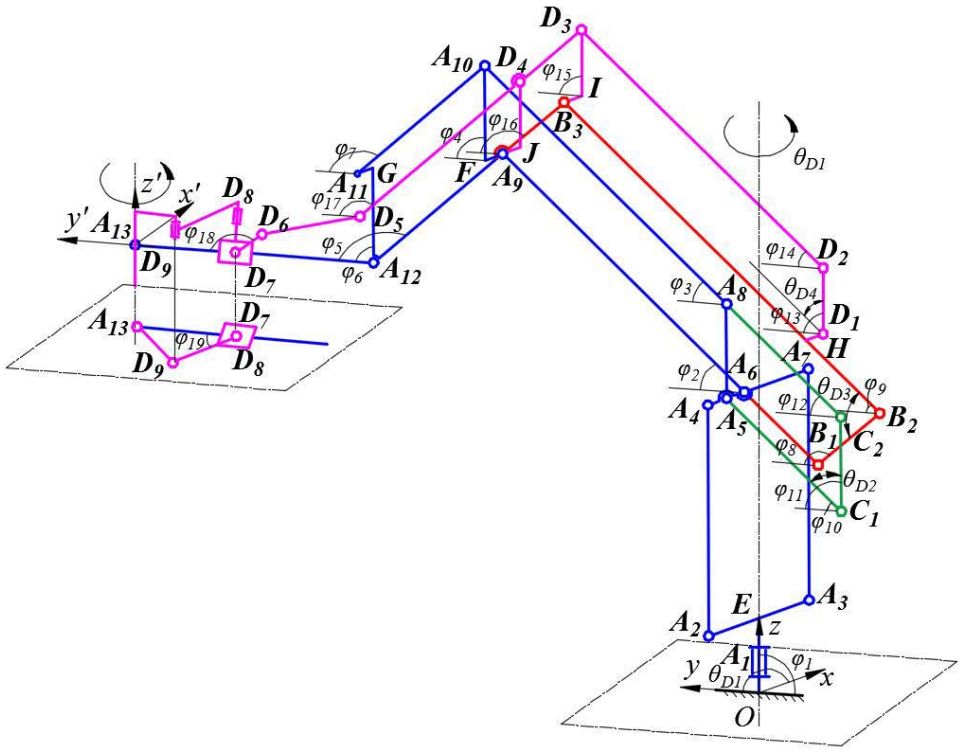

FIGURE 2. Evolution law of the branch chain hierarchical relationship of the CM robot.

a multi-loop mechanism, and the purpose of the branch chain $A_5A_8A_{10}A_{11}$ is to control the end member $A_{12}A_{13}$ in order to remain horizontal. In Figure 1, $o-xyz$ is the overall coordinate system, A_i $(i = 1, 2, \cdots, 13)$ represents the number of kinematic pairs, φ_i $(i = 1, 2, \cdots, 7)$ is the included angle between each component and the horizontal direction,

and θ_{ij} $(i = A, B, C, D, j = 1, 2, 3, 4)$ represents the driving angle of the j^{th} motor of configuration i. Each motor and reducer of the mechanism are installed at the revolute pair; specifically, motor 1 controls the rotating movement of the entire robot, motor 2 controls the rotation of beam A_6A_9, motor 3 controls the rotation of forearm A_9A_{12}, and motor 4 controls the rotation of end gripper. In this paper, taking the series robot shown in Figure 1 as configuration A of the CM robot, we can obtain the following constraints:

$$\begin{cases} L_{A_2A_3} = L_{A_4A_7} \\ L_{A_2A_4} = L_{A_3A_7} \\ L_{A_6A_9} = L_{A_8A_{10}} \\ L_{A_9A_{12}} = L_{A_{10}A_{11}} \\ \varphi_1 = \varphi_4 = \varphi_6 = \pi/2 \\ \varphi_2 = \varphi_3 \\ \varphi_5 = \varphi_7 \end{cases} \tag{1}$$

where $L_{A_iA_j}$ $(i, j = 1, 2, \cdots, 8)$ represents the member length, and $\varphi_2 = \theta_{A2}$, $\varphi_5 = \pi - \theta_{A3}$.

B. EVOLUTION PROCESS OF CM ROBOT CONFIGURATION

[45] first proposed a new type of H-P mechanism according to the tree–rattan parasitic relationship in nature, classified the parasitic branch chains of the H-P mechanism, and obtained a variety of reconfigurable parasitic mechanisms. Both the CM robot and H-P mechanism have obvious hierarchical relationships. In other words, the host mechanism is the main support of the entire mechanism and has the entire DOF of the mechanism, and the branch chain mechanism is connected with the host mechanism through kinematic pairs or components. According to the hierarchical relationship of the CM robot, the branch chain can be continuously added to the host mechanism or to the upper branch chain in order to obtain CM mechanisms with different configurations. Therefore, on the basis of the hierarchical relationship of the CM robot, taking configuration A shown in Figure 1 as the host mechanism, three new CM robot configurations can be obtained, as shown in Figure 2. It is worth noting that the blue part represents configuration A (including symbols), configuration A plus the red part is configuration B, configuration B plus the green part is configuration C, and the entire schematic diagram denotes configuration D.

According to the evolution law of the CM mechanism, the three new CM robots have 4 DOFs and are driven by four motors. The hierarchical relationship of the CM mechanism is reflected in two aspects: one is that the motor and reducer move to or near the frame, which can reduce the moment of inertia of the CM robot; the other is that the increase in the branch chain can improve the structural stiffness of the robot and reduce the residual vibration. On the basis of satisfying the constraints of equation (1), configuration B satisfies the following constraints:

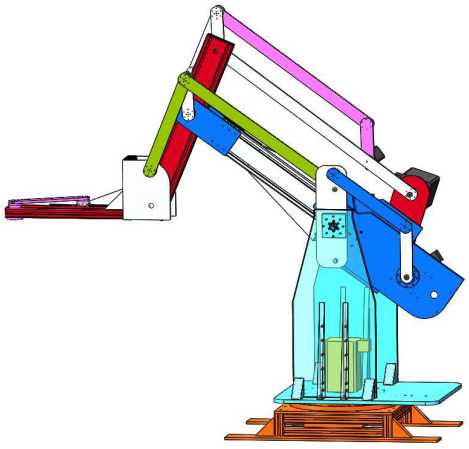

FIGURE 3. Virtual prototype of the CM robot.

$$\begin{cases} L_{A_6A_9} + L_{A_6B_1} = L_{B_2B_3} \\ L_{B_1B_2} = L_{A_9B_3} \\ \varphi_2 = \varphi_9 \\ \varphi_5 = \varphi_8 \end{cases} \tag{2}$$

where $\varphi_2 = \theta_{B2}, \varphi_8 = \pi + \theta_{B2} - \theta_{B3}$. Configuration C satisfies not only the following constraints but also the conditions of equations (1) and (2):

$$\begin{cases} L_{A_5C_1} = L_{A_8C_2} \\ L_{A_5A_8} = L_{C_1C_2} \\ \varphi_2 = \varphi_{12} = \varphi_{10} \end{cases} \tag{3}$$

Similarly, on the basis of satisfying the constraints of equations (1)-(3), configuration D also satisfies the following constraints:

$$\begin{cases} L_{D_1D_2} = L_{ID_3} = L_{JD_4} \\ L_{HB_3} = L_{D_2D_3} \\ \varphi_2 = \varphi_{12} = \varphi_{10} \end{cases} \tag{4}$$

where $\varphi_2 = \pi/2 - \theta_{C2}$, $\varphi_8 = \pi + \theta_{B2} - \theta_{B3}$. According to the geometric dimensions of the CM robot, the 3D model diagram and physical prototype of the CM robot corresponding to configuration D are obtained, as shown in Figure 3 and Figure 4.

III. MOMENT OF INERTIA OF THE CM ROBOT

This section gives the calculation method for the moment of inertia of the CM robot. A large moment of inertia will lead to a poor dynamic performance of the robot and easily produces a large residual vibration. Therefore, it is necessary to calculate the moment of inertia of the CM robot with different branch chains. As shown in Figure 1 and Figure 2, o-xyz is the global coordinate system of the CM robot, and A_{13}-$x'y'z'$ is the local coordinate system of the

FIGURE 4. Physical prototype of the CM robot.

end output component of the CM robot. The four configurations of the CM robot have 4 DOFs, including two rotations around the x-axis and Z-axis and two translations of the y-direction and z-direction. Therefore, when calculating the moment of inertia of the CM robot, it is necessary to consider the moment of inertia for different rotating axes. Let $D_1\,(0, y_1, z_1)$ be a point in the YOZ plane and $D_2\,(x_2, y_2, 0)$ be a point in the XOY plane. Considering the moment of inertia caused by the concentrated mass of the driving motor, the minimum moment of inertia of the CM robot in the two planes is:

$$\begin{cases} J_{x\min} = \sum_{i=1}^{N}\left(\int\left((y_1-y_i)^2+(z_1-z_i)^2\right)dm_i\right) \\ \qquad\quad +\sum_{j=1}^{4}\left(\left(y_1-y_j\right)^2+\left(z_1-z_j\right)^2\right)m_j \\ J_{z\min} = \sum_{i=1}^{N}\left(\int\left((x_2-x_i)^2+(y_2-y_i)^2\right)dm_i\right) \\ \qquad\quad +\sum_{j=1}^{4}\left(\left(x_1-x_j\right)^2+\left(y_1-y_j\right)^2\right)m_j \end{cases} \tag{5}$$

where N is the number of members, represents the mass of component i, and m_j represents the mass of motor j. The coordinates of the driving joint where the motor is located are (x_j, y_j, z_j). It is assumed that the masses of each link of the four configurations of the CM robot are evenly distributed. When $y_1 = z_1 = x_2 = y_2 = 0$, and considering the concentrated mass of the motor at the driving joint, the moment of inertia of each CM robot about the x-axis and z-axis can be obtained from equation (5):

$$\begin{cases} J_x = \sum_{i=1}^{N}\left(\int\left(y_i^2+z_i^2\right)dm_i\right)+\sum_{j=1}^{4}\left(y_j^2+z_j^2\right)m_j \\ J_z = \sum_{i=1}^{N}\left(\int\left(x_i^2+y_i^2\right)dm_i\right)+\sum_{j=1}^{4}\left(x_j^2+y_j^2\right)m_j \end{cases} \tag{6}$$

IV. DYNAMIC MODEL OF THE CM ROBOT

The mathematical model of the residual vibration of the CM robot and its fitting method are introduced in this section.

A. MODELLING STEPS OF THE DYNAMIC MODEL OF THE CM ROBOT

Figure 5 is a flowchart of the dynamic model modeling of the CM robot. The following details the steps:

Step 1: Configurations A, B, C and D of the CM robot are selected as the research objects. For each configuration, a single extreme working pose is selected for the analysis.

Step 2: The initial FE model of the CM robot virtual prototype is established in ADAMS software. The residual vibration of the CM robot by impulse excitation is solved as the initial condition for theoretical modeling.

Step 3: According to the length of each link, the length of the flexible 3D beam element is reasonably divided to calculate the total number of units for each configuration of the CM robot.

Step 4: In the process of theoretical modeling, the influence of the irregular boundary and stiffener of the CM robot on the residual vibration is ignored. Therefore, the Monte Carlo method is used to fit the area moment of inertia and the polar moment of inertia of each element. Based on the initial FE model analysis results of the CM robot, the fitting order of the area moment of inertia and polar moment of inertia is determined. Because the stiffness of the CM robot in the Y-direction and Z-direction is large, it is approximately simplified according to 90 deformations, so the fitting factors $F_y = 0.09$, $F_z = 0.09$ and $F_I = 0.09$ are determined.

Step 5: The beam element is assumed to be Timoshenko SBE. Then, the kinetic energy and strain energy of the beam element are calculated, and the dynamic equation of the SBE is established by using the Lagrange equation.

Step 6: The rigid body motion constraints, elastic deformation constraints and force constraints of the CM robot are analyzed, and the constraint equations of the system are obtained.

Step 7: The mass matrix and stiffness matrix of each element are assembled to obtain the mass matrix and the stiffness matrix of the CM robot system.

Step 8: According to the displacement boundary conditions in the constraint equation of the system, the mass matrix and stiffness matrix of the system are modified to eliminate the rigid degree of freedom of node displacement, and the modified system dynamic equation is obtained.

Step 9: The residual vibration response of configuration D of the CM robot under pulse excitation is measured experimentally. The Rayleigh damping coefficients and are fitted by the Monte Carlo method to obtain the damping matrix of the system.

Step 10: The modified dynamic equation of configuration D of the CM robot is obtained, and the residual vibration response of the end link of the CM robot is solved using a numerical method. Step 11: The FE model of the virtual

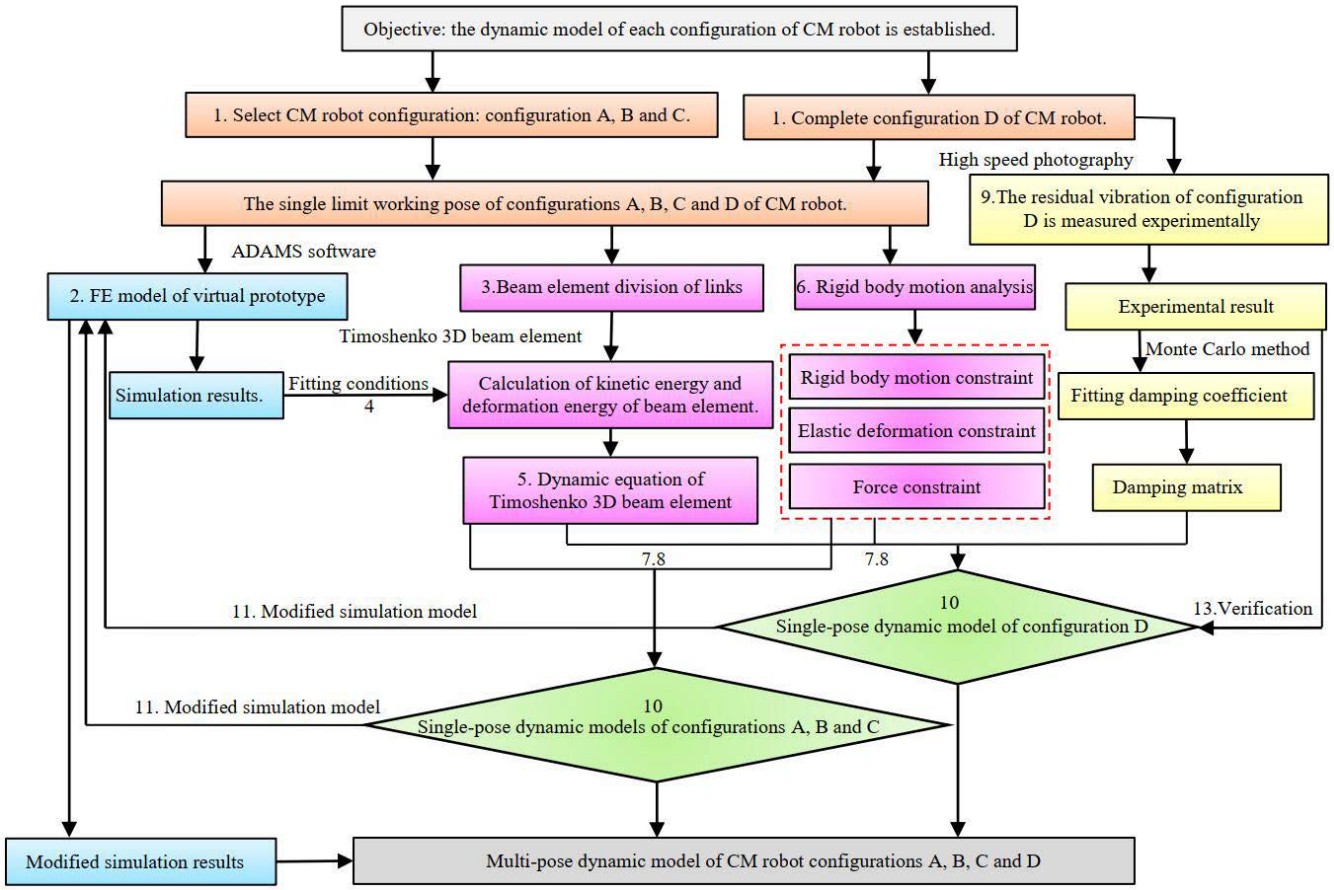

FIGURE 5. Flowchart of the dynamic modeling of the CM robot.

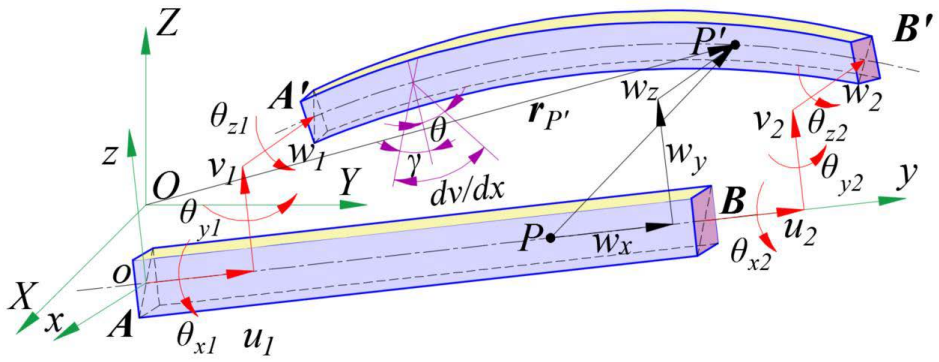

FIGURE 6. Timoshenko SBE model.

prototype established in step 2 is modified to obtain the residual vibration response of the CM robot under the same pulse excitation.

Step 12: Repeat steps 2 to 10 for different CM robot configurations. Verify the correctness of the theoretical modeling of the four configurations.

B. TIMOSHENKO SBE MODEL

The Timoshenko SBE model is shown in Figure 6, where XOY is the system coordinate system and is the local coordinate system of the beam element. Any point on the SBE is after deformation. It is assumed that the generalized coordinate vector e_f of the SBE is:

$$e_f = \left[u_1\ v_1\ w_1\ \theta_{x1}\ \theta_{y1}\ \theta_{z1}\ u_2\ v_2\ w_2\ \theta_{x2}\ \theta_{y2}\ \theta_{z2}\right]^T \quad (7)$$

where u_i, v_i and w_i are the displacements of node i along the local coordinate direction, and θ_{xi}, θ_{yi} and θ_{zi} are the rotation angles of node i around the three coordinate axes. In addition, θ_{xi} represents the corner of the section.

The displacement of point P on any cross-section in the SBE is expressed in generalized coordinates as:

$$\begin{cases} w_x(\bar{x}_P, t) = \sum_i \phi_i(\bar{x}_P) u_g \\ w_y(\bar{x}_P, t) = \sum_{j,k} \left(\phi_j(\bar{x}_P) v_g + \phi_k(\bar{x}_P) \theta_{yg}\right) \\ w_z(\bar{x}_P, t) = \sum_p \left(\phi_p(\bar{x}_P) w_g + \phi_s(\bar{x}_P) \theta_{zg}\right) \\ \theta_x(\bar{x}_P, t) = \sum_r \phi_r(\bar{x}_P) \theta_{xg} \end{cases} \tag{8}$$

where $i = 1, 7, g = 1, 2, j = 2, 8, k = 6, 12, p = 3, 9, s = 5, 11, r = 4, 10$, w_x, w_y and w_z represent the elastic displacement along the corresponding coordinate axis after point P of the beam element is deformed, respectively, θ_x represents the elastic rotation angle along the x-axis direction, and $\phi(\bar{x}_P)$ is a shape function related to the geometric parameters of SBE.

The links of the CM robot are subjected to an axial force, bending moment, torque, and shear force. It can be considered that all links are Timoshenko SBE. The cross-section of the Timoshenko SBE perpendicular to the centerline of the beam before deformation is not perpendicular to the centerline of the beam after deformation. The deformation diagram of the beam element is shown in Figure 6, and the corner of the cross section is as follows:

$$\theta = \frac{dv}{dx} - \gamma \tag{9}$$

According to the generalized Hooke's law, we can obtain:

$$\begin{cases} E\varepsilon_x = \sigma_x - v\left(\sigma_y + \sigma_z\right) \\ E\varepsilon_y = \sigma_y - v\left(\sigma_z + \sigma_x\right) \\ E\varepsilon_z = \sigma_z - v\left(\sigma_x + \sigma_y\right) \\ G\gamma_{xy} = \tau_{xy} \\ G\gamma_{yz} = \tau_{yz} \\ G\gamma_{zx} = \tau_{zx} \end{cases} \tag{10}$$

where E is the elastic modulus; G is the shear modulus; and v is Poisson's ratio.

For a micro element dV, the stored strain energy is:

$$dU = \frac{1}{2}(\sigma_x\varepsilon_x + \sigma_y\varepsilon_y + \sigma_z\varepsilon_z + \tau_{xy}\gamma_{xy} + \tau_{yz}\gamma_{yz} + \tau_{zx}\gamma_{zx})dxdydz \tag{11}$$

where σ_x, σ_y and σ_z are normal stress components; τ_{xy}, τ_{yz} and τ_{zx} are shear stress components; ε_x, ε_y and ε_z are normal strain components; and γ_{xy}, γ_{yz} and γ_{zx} are shear strain components. Substituting equation (10) into equation (11), the strain energy of Timoshenko SBE considering axial force, torque, transverse force and bending moment is as follows:

$$\begin{aligned} U = {} & \frac{b}{2}\int_0^l \int_{-\frac{h}{2}}^{\frac{h}{2}} \varepsilon_x^T E\varepsilon_x dydx + \frac{\rho}{2}\int_0^l \int_{-\frac{h}{2}}^{\frac{h}{2}} \alpha^T E\alpha dydx \\ & + \frac{b}{2}\int_0^l \int_{-\frac{h}{2}}^{\frac{h}{2}} \kappa_z^T E\kappa_z dzdx + \frac{h}{2}\int_0^l \int_{-\frac{b}{2}}^{\frac{b}{2}} \kappa_y^T E\kappa_y dydx \\ & + \frac{1}{2}b\int_0^l \int_{-\frac{h}{2}}^{\frac{h}{2}} \gamma^T \frac{G}{k}\gamma dydx \end{aligned} \tag{12}$$

By substituting the geometric relationship of the beam element deformation into equation (12), we can obtain:

$$\begin{aligned} U = {} & \frac{1}{2}\int_0^l EA\left(\frac{du}{dx}\right)^2 dx + \frac{1}{2}\int_0^l GJ\left(\frac{d\theta_x}{dx}\right)^2 dx \\ & + \frac{1}{2}\int_0^l EI_y\left(-\frac{d\theta}{dx}\right)^2 dx + \frac{1}{2}\int_0^l EI_z\left(-\frac{d\theta}{dx}\right)^2 dx \\ & + \frac{1}{2}\int_0^l \frac{GA}{k}\left(\frac{dv}{dx} - \theta\right)^2 dx \end{aligned} \tag{13}$$

where $I_y = \int_{-\frac{h}{2}}^{\frac{h}{2}} bz^2 dz$, $I_z = \int_{-\frac{b}{2}}^{\frac{b}{2}} hy^2 dy$, $A = \int_{-\frac{h}{2}}^{\frac{h}{2}} bdz$, $J = \int_{-\frac{h}{2}}^{\frac{h}{2}} \int_{-\frac{b}{2}}^{\frac{b}{2}} \rho^2 dydz$, where b, h and l are the width, height, and length of the SBE, respectively, I_y and I_z are the area moments of inertia of the SBE to the y-axis and z-axis, respectively, G is the shear modulus of the SBE, F is the cross-sectional area of SBE, and k is the correction factor, which is introduced because the strain and stress of the actual shear deformation are not uniformly distributed, where $k = 6/5$.

According to the deformation energy of Timoshenko SBE, we can obtain the element stiffness matrix:

$$\mathrm{K}^e = \begin{bmatrix} K_{11} & K_{12} \\ K_{21} & K_{22} \end{bmatrix} \tag{14}$$

where

$$K_{11} = K_{22} = \begin{bmatrix} a_1 & & & & & \\ & a_2 & & & & a_3 \\ & & a_2 & & -a_3 & \\ & & & a_4 & & \\ & & -a_3 & & a_5 & \\ & a_3 & & & & a_6 \end{bmatrix}$$

$$K_{12} = K_{21} = \begin{bmatrix} -a_1 & & & & & \\ & -a_2 & & & & a_3 \\ & & -a_2 & & -a_3 & \\ & & & -a_4 & & \\ & & a_3 & & a_7 & \\ & -a_3 & & & & a_8 \end{bmatrix}$$

$$a_1 = \frac{EA}{l}, \quad a_2 = \frac{GA}{4kl}, \quad a_3 = -\frac{GA}{2k}, \quad a_4 = \frac{GJ}{l},$$
$$a_5 = \frac{GAl}{4k} + \frac{GI_y}{l}, \quad a_6 = \frac{GAl}{4k} + \frac{GI_z}{l},$$
$$a_7 = \frac{GAl}{4k} - \frac{GI_y}{l}, \quad a_8 = \frac{GAl}{4k} - \frac{GI_z}{l}.$$

It is assumed that the mass of the SBE is concentrated on the axis. The kinetic energy expression of Timoshenko SBE is as follows:

$$\begin{aligned} T = {} & \frac{1}{2}\int_{-\frac{h}{2}}^{\frac{h}{2}} \int_{-\frac{b}{2}}^{\frac{b}{2}} \dot{\mathrm{u}}^T \rho \dot{\mathrm{u}} l dydz + \frac{1}{2}\int_0^l \int_{-\frac{h}{2}}^{\frac{h}{2}} \dot{\mathrm{v}}^T \rho \dot{\mathrm{v}} bdzdx \\ & + \frac{1}{2}\int_0^l \int_{-\frac{b}{2}}^{\frac{b}{2}} \dot{\mathrm{w}}^T \rho \dot{\mathrm{w}} hdydx + \frac{1}{2}\int_0^{l_e} \dot{\theta}_x^2(x,t)\, dJ_c \end{aligned} \tag{15}$$

where ρ is the material density, $\dot{\mathrm{u}}$, $\dot{\mathrm{v}}$ and $\dot{\mathrm{w}}$ are absolute velocity arrays along three coordinate axes, $\dot{\mathrm{v}} = \dot{\mathrm{v}}_s + \dot{\mathrm{v}}_t$, $\dot{\mathrm{v}}_s$ is the transverse velocity caused by bending deformation,

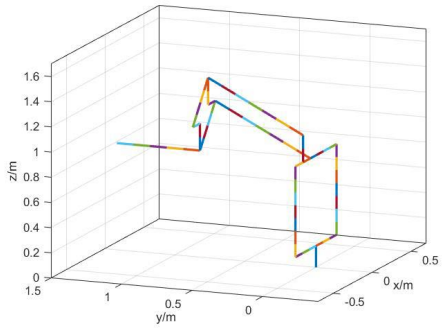

(a) Configuration A without a branched chain.

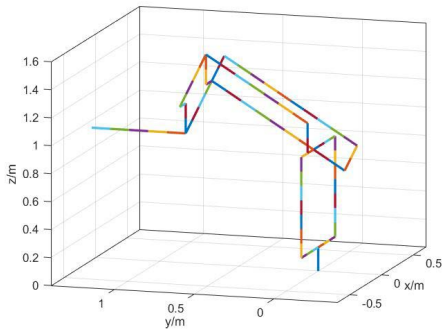

(b) Configuration B with one branched chain.

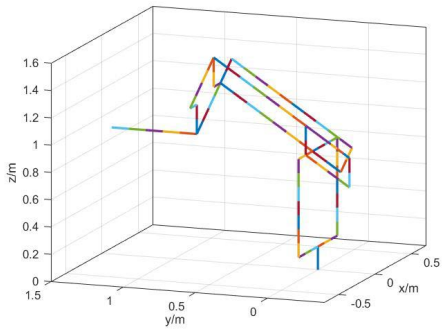

(c) Configuration C with two branched chains.

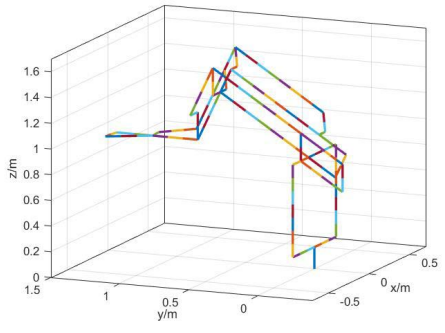

(d) Configuration D with three branched chains.

FIGURE 7. Schematic diagram of the element division of FEA.

and $\dot{v}_t$ is the lateral velocity caused by shear deformation. By substituting equation (7) and the shape function $\phi(\bar{x}_P)$ into equation (15), we can obtain the SBE mass matrix as follows:

$$\mathrm{M}^e = \frac{\rho A l}{6}\begin{bmatrix} M_{11} & M_{12} \\ M_{21} & M_{22} \end{bmatrix} \tag{16}$$

where

$$M_{11} = M_{22} = \begin{bmatrix} 2 & & & & & & \\ & 2 & & & & & \\ & & 2 & & & & \\ & & & 2J/A & & & \\ & & & & l & & \\ & & & & & l & \end{bmatrix}$$

$$M_{12} = M_{21} = \begin{bmatrix} 1 & & & & & & \\ & 1 & & & & & \\ & & 1 & & & & \\ & & & J/A & & & \\ & & & & 0 & & \\ & & & & & 0 & \end{bmatrix}$$

When the Lagrange equation is applied to the SBE, we can obtain:

$$\frac{d}{dt}\left(\frac{\partial T}{\partial \dot{\mathrm{e}}_f}\right) - \frac{\partial T}{\partial \mathrm{e}_f} + \frac{\partial U}{\partial \mathrm{e}_f} = \mathrm{F} + \mathrm{Q} \tag{17}$$

where F is the generalized force array of the applied load, and Q represents the array of interaction forces between elements. The derivatives of equation (13) and equation (15) are calculated at the same time and substituted into equation (17), and the viscous damping theory is used to take the influence of damping into account. The dynamic model of SBE is as follows:

$$\sum_{j=1}^{12} M_{ij}^e \ddot{e}_f + \sum_{j=1}^{12} C_{ij}^e \dot{e}_f + \sum_{j=1}^{12} K_{ij}^e e_f = F_i + Q_i \tag{18}$$

where $i = 1, 2, \cdots, 12$.

Equation (18) is written in matrix form as follows:

$$\mathrm{M}^e\ddot{\mathrm{e}}_f + \mathrm{C}^e\dot{\mathrm{e}}_f + \mathrm{K}^e\mathrm{e}_f = \mathrm{F} + \mathrm{Q} \tag{19}$$

C. DYNAMIC MODEL OF SBE IN THE SYSTEM COORDINATE SYSTEM

First, the CM robot of each configuration is divided into elements, and the appropriate number of elements is divided according to the link length of the configuration. In Figure 7, each color segment is an element. The number of elements and nodes of each configuration of the CM robot are shown in Table 1.

Equation 19 is the SBE dynamic model, which is established in the element local coordinate system and needs to be converted to the system coordinate system to assemble the element stiffness matrix and mass matrix into the stiffness

TABLE 1. Division of each configuration element of the CM robot.

Configura -tion name	Number of links	Number of elements	Number of nodes
A	15	62	60
B	19	78	75
C	22	88	84
D	36	122	114

matrix and mass matrix of the system. For Timoshenko SBE, the transformation matrix R between the local coordinate system and the system coordinate system is as follows [46]:

$$\mathrm{R} = \begin{bmatrix} \mathrm{t} & 0 & 0 & 0 \\ 0 & \mathrm{t} & 0 & 0 \\ 0 & 0 & \mathrm{t} & 0 \\ 0 & 0 & 0 & \mathrm{t} \end{bmatrix} \tag{20}$$

where,

$$\mathrm{t} = \begin{bmatrix} \cos(x,\bar{x}) & \cos(x,\bar{y}) & \cos(x,\bar{z}) \\ \cos(y,\bar{x}) & \cos(y,\bar{y}) & \cos(y,\bar{z}) \\ \cos(z,\bar{x}) & \cos(z,\bar{y}) & \cos(z,\bar{z}) \end{bmatrix} \tag{21}$$

The first line of equation (21) can be obtained by using the node coordinates:

$$\begin{cases} \cos(x,\bar{x}) = \dfrac{\bar{x}_2 - \bar{x}_1}{l} \\ \cos(x,\bar{y}) = \dfrac{\bar{y}_2 - \bar{y}_1}{l} \\ \cos(x,\bar{z}) = \dfrac{\bar{z}_2 - \bar{z}_1}{l} \\ l = \sqrt{(\bar{x}_2 - \bar{x}_1)^2 + (\bar{y}_2 - \bar{y}_1)^2 + (\bar{z}_2 - \bar{z}_1)^2} \end{cases} \tag{22}$$

Other lines of equation (21) can be obtained by using the auxiliary reference coordinate system $o' - x'y'z'$. The following is the conversion matrix between the auxiliary reference coordinate system $o' - x'y'z'$ and the overall coordinate system $O - XYZ$ of the system:

$$\mathrm{t}_1 = \begin{bmatrix} l & m & n \\ -\dfrac{m}{\lambda} & \dfrac{l}{\lambda} & 0 \\ -\dfrac{nl}{\lambda} & -\dfrac{mn}{\lambda} & \lambda \end{bmatrix} \tag{23}$$

where

$$\begin{cases} \cos(x,\bar{x}) = \dfrac{(\bar{x}_j - \bar{x}_i)}{\sqrt{(\bar{x}_j - \bar{x}_i)^2 + (\bar{y}_j - \bar{y}_i)^2 + (\bar{z}_j - \bar{z}_i)^2}} = l \\ \cos(x,\bar{y}) = \dfrac{(\bar{y}_j - \bar{y}_i)}{\sqrt{(\bar{x}_j - \bar{x}_i)^2 + (\bar{y}_j - \bar{y}_i)^2 + (\bar{z}_j - \bar{z}_i)^2}} = m \\ \cos(x,\bar{z}) = \dfrac{(\bar{z}_j - \bar{z}_i)}{\sqrt{(\bar{x}_j - \bar{x}_i)^2 + (\bar{y}_j - \bar{y}_i)^2 + (\bar{z}_j - \bar{z}_i)^2}} = n \\ \lambda = \sqrt{l^2 + m^2} \end{cases}$$

The following is the conversion matrix between the auxiliary reference coordinate system $o' - x'y'z'$ and the element local coordinate system $o - xyz$:

$$\mathrm{t}_2 = \begin{bmatrix} 1 & 0 & 0 \\ 0 & \cos\alpha & \sin\alpha \\ 0 & -\sin\alpha & \cos\alpha \end{bmatrix} \tag{24}$$

where A is the angle between the Y-axis of the local coordinate system of the element and the Y'-axis of the auxiliary reference coordinate system. t in equation (21) is as follows:

$$\mathrm{t} = \mathrm{t}_2\mathrm{t}_1 = \begin{bmatrix} 1 & 0 & 0 \\ 0 & \cos\alpha & \sin\alpha \\ 0 & -\sin\alpha & \cos\alpha \end{bmatrix} \begin{bmatrix} l & m & n \\ -\dfrac{m}{\lambda} & \dfrac{l}{\lambda} & 0 \\ -\dfrac{nl}{\lambda} & -\dfrac{mn}{\lambda} & \lambda \end{bmatrix} \tag{25}$$

If the x of the SBE is parallel to the z-axis of the overall coordinate system, then the transformation matrix t_2 is as follows:

$$\mathrm{t}_2 = \begin{bmatrix} 0 & 0 & 1 \\ -\sin\alpha & \cos\alpha & 0 \\ -\cos\alpha & -\sin\alpha & 0 \end{bmatrix} \tag{26}$$

The following is the relationship between the element node displacement in the local coordinate system and the element node displacement in the overall coordinate system:

$$\mathrm{e}_f = \mathrm{T}\bar{\mathrm{e}}_f \tag{27}$$

Substituting equation (27) into equation (19) and multiplying both sides by T^T, the dynamic model of SBE in the system coordinate system can be obtained as follows:

$$\bar{\mathrm{M}}^e\ddot{\bar{\mathrm{e}}}_f + \bar{\mathrm{C}}^e\dot{\bar{\mathrm{e}}}_f + \bar{\mathrm{K}}^e\mathrm{e}_f = \bar{\mathrm{F}}^e + \bar{\mathrm{Q}}^e \tag{28}$$

where $\bar{\mathrm{M}}^e = \mathrm{T}^T\mathrm{M}^e\mathrm{T}$ is the element mass matrix in system coordinates, $\bar{\mathrm{C}}^e = \mathrm{T}^T\bar{\mathrm{C}}^e\mathrm{T}$ denotes the element damping matrix in system coordinates, $\bar{\mathrm{K}}^e = \mathrm{T}^T\bar{\mathrm{K}}^e\mathrm{T}$ represent the element stiffness matrix in system coordinates, $\bar{\mathrm{F}}^e = \mathrm{T}^T\mathrm{F}^e$ is the external load force vector array in system coordinates, and $\bar{\mathrm{Q}}^e = \mathrm{T}^T\mathrm{Q}^e$ denote the vector array of interaction forces between elements in system coordinates.

D. DYNAMIC MODEL OF CM ROBOT

The element dynamic model in the global coordinate system is discrete and needs to be assembled. The dynamic equations of each SBE are superimposed according to the global coordinate sequence of the overall number, and the dynamic models of the four configurations of the CM robot can be obtained as follows:

$$\mathrm{M}_i\ddot{\bar{\mathrm{e}}}_f + \mathrm{C}_i\dot{\mathrm{e}}_f + \mathrm{K}_i\mathrm{e}_f = \mathrm{F}_i(t) + \mathrm{Q}_i(\theta_{i1},\theta_{i2},\theta_{i3},\theta_{i4}) \tag{29}$$

where $i = A, B, C, D$. $\mathrm{M}_i = \sum_{k=1}^{Nu}\bar{\mathrm{M}}_k^e$ is the mass matrix of CM robot configuration i, $\mathrm{C}_i = \sum_{k=1}^{Nu}\bar{\mathrm{C}}_k^e$ denotes the damping matrix of CM robot configuration i, $\mathrm{K}_i = \sum_{k=1}^{Nu}\bar{\mathrm{K}}_k^e$ represents the stiffing matrix of CM robot configuration i,

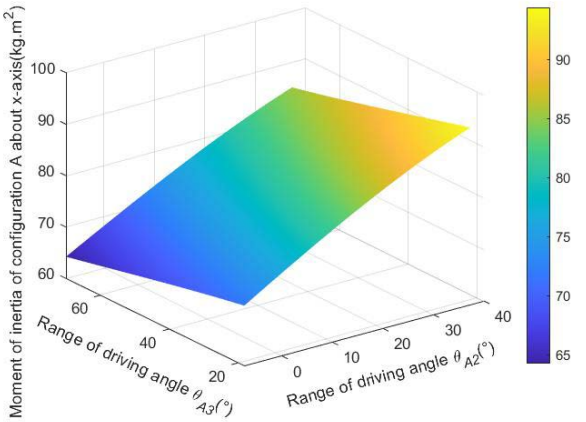

(a) Moment of inertia of configuration A about the x-axis.

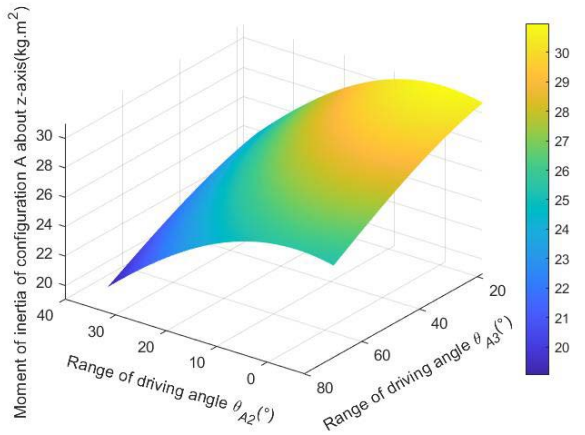

(b) Moment of inertia of configuration A about the z-axis.

FIGURE 8. Moment of inertia of configuration A without a branched chain.

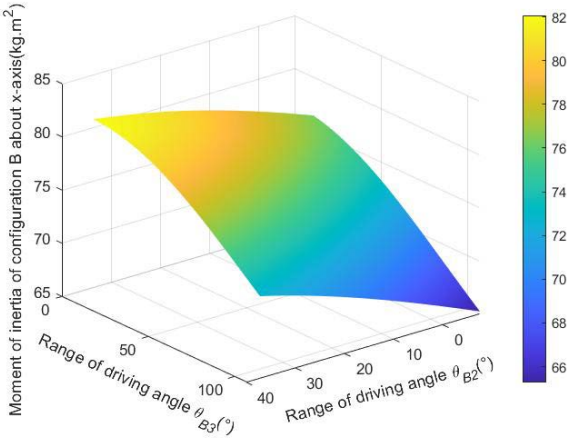

(a) Moment of inertia of configuration B about the x-axis.

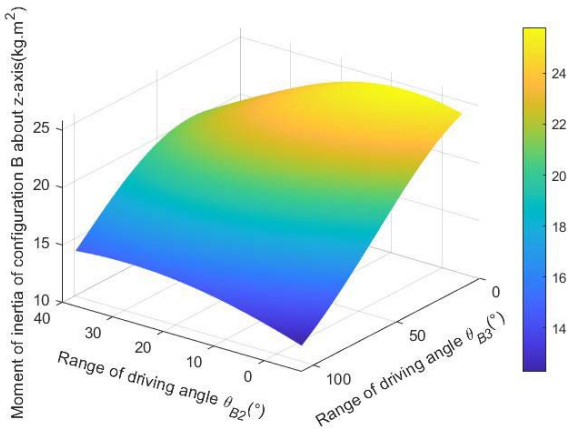

(b) Moment of inertia of configuration B about the z-axis.

FIGURE 9. Moment of inertia of configuration B with one branched chain.

$F_i(t)$ is the external load force vector array of configuration i, $Q_i(\theta_{i1}, \theta_{i2}, \theta_{i3}, \theta_{i4})$ denotes the inertial force array of the system, and Nu represents the total number of system elements.

E. FITTING THE ORDER OF BOUNDARY CHARACTERISTIC PARAMETERS

Timoshenko SBE is used to establish the theoretical model, but the effects of the bearing clearance, irregular boundary and stiffener of the CM robot on the dynamic performance are not considered. The stiffener has a significant effect on the residual vibration of the robot. Therefore, to allow the theoretical modeling to represent the actual situation, the boundary characteristic parameters that significantly affect the dynamics of the CM robot are fitted according to the fitting method proposed in the literature [46]. According to equation (13), the bearing clearance, irregular boundary of the link and stiffener have little influence on the tensile and compressive deformation of SBE and have a great influence on other deformations. The boundary characteristic parameters are $I_y = f_{I_y} I'_y$, $I_z = f_{I_z} I'_z$ and $J = f_J J'$. Therefore, according to the dynamic simulation analysis results of the CM robot, we can determine the order of fitting parameters f_{I_y}, f_{I_z} and f_J, as shown in Table 2.

In each configuration of the CM robot, a pulse excitation of -50N along the Z direction is applied at the end point A_{13}, that is, $F_{initial} = [0, 0 - 50N]^T$. Taking the amplitude of the residual vibration as the objective function, the boundary characteristic parameters are fitted by the Monte Carlo method. By comparing and analyzing the change in the residual vibration amplitude A at the end of the CM robot, the size and order of the fitting parameters are determined. By comparing the variation in the residual vibration amplitude $e_{60} = [u_{60}, v_{60}, w_{60}]^T$ at the end of the CM robot, the size and order of the fitting parameters are determined.

TABLE 2. Influence of the boundary characteristic parameters of configuration D on residual vibration.

Configuration type	Element type	Fitting reference	Boundary characteristic parameters that significantly affect amplitude	Boundary characteristic parameters that significantly affect the period
Configuration D	Timoshenko SBE	Simulation result	f_{Iy}, f_{Iz}, f_J	f_A

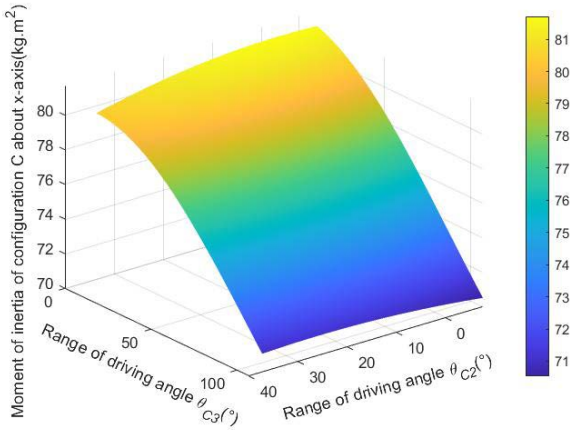

(a) Moment of inertia of configuration C about the x-axis.

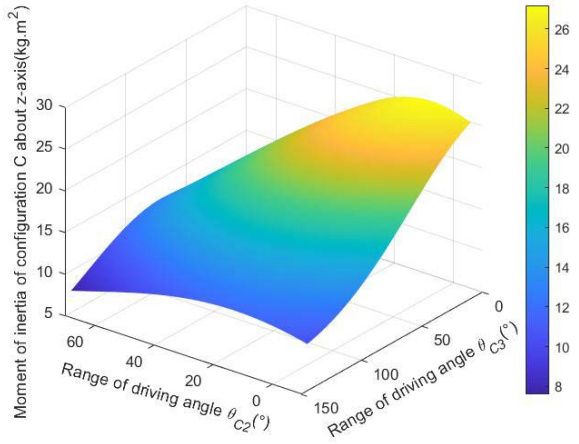

(b) Moment of inertia of configuration C about the z-axis.

FIGURE 10. Moment of inertia of configuration C with two branched chains.

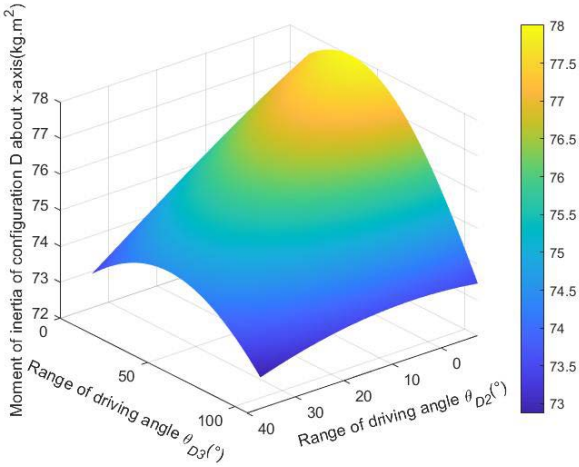

(a) Moment of inertia of configuration D about the x-axis.

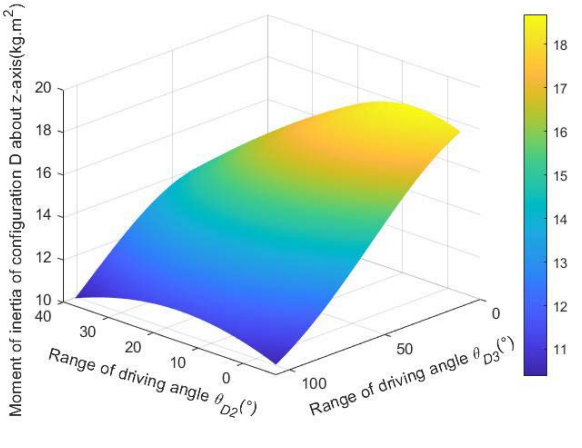

(b) Moment of inertia of configuration D about the z-axis.

FIGURE 11. Moment of inertia of configuration D with three branched chains.

V. NUMERICAL CALCULATION OF THE MOMENT OF INERTIA

A. GEOMETRIC PARAMETERS OF THE CM ROBOT

As shown in Figures 1-4, L_{ij} is the length of each link in configuration i. A_{ij} is the cross-sectional area of each link, I_{yij} is the cross-sectional moment of inertia of each link of configuration i in the xoz coordinate plane, I_{zij} is the cross-sectional moment of inertia of each link of configuration i in the xoy coordinate plane, and $J_{ij} = I_{yij} + I_{zij}$ is the polar moment of inertia of each member of configuration i. The CM robot was fabricated with aluminum alloy. The geometric parameters of the four configurations of the CM robot are shown in Table 3.

The mass of the motor is the main factor affecting the moment of inertia. Each CM robot has four drive motors. The mass of the driving motor is shown in Table 4.

B. COMPARATIVE ANALYSIS OF THE MOMENT OF INERTIA OF THE CM ROBOT

The moment of inertia of the robot is determined by the driving torque of the robot. A large moment of inertia requires a large driving torque, and a large driving torque is provided

TABLE 3. Geometric parameters of CM robots.

Link name	Link length (m)	Cross sectional area (m^2)	Cross section moment of inertia I_y (m^4)	Cross section moment of inertia I_z (m^4)	Number of division elements
L_{OE}	0.17	10.991×10^{-2}	36.26×10^{-4}	36.26×10^{-4}	1
$L_{A_2A_3}$	0.532	10.5×10^{-3}	1.969×10^{-7}	4.288×10^{-4}	6
$L_{A_2A_4}=L_{A_3A_7}$	0.72	6.05×10^{-3}	2.02×10^{-7}	4.613×10^{-5}	7
$L_{A_4A_7}$	0.532	9.293×10^{-3}	8.29×10^{-6}	8.29×10^{-6}	7
$L_{A_5A_8}$	0.215	1.3×10^{-3}	1.08×10^{-8}	1.83×10^{-6}	2
$L_{A_6A_9}$	0.78	1.1×10^{-3}	1.699×10^{-6}	2.366×10^{-7}	7
$L_{A_8A_{10}}$	0.78	0.224×10^{-3}	3.34×10^{-9}	5.55×10^{-8}	7
$L_{A_{10}F}$	0.215	0.224×10^{-3}	3.34×10^{-9}	5.55×10^{-8}	2
$L_{A_9F}=L_{A_{11}G}$	0.093	1.96×10^{-3}	3.12×10^{-7}	3.12×10^{-7}	1
$L_{A_9A_{12}}$	0.42	1.1×10^{-3}	1.699×10^{-6}	2.366×10^{-7}	4
$L_{A_{10}A_{11}}$	0.42	0.224×10^{-3}	3.34×10^{-9}	5.55×10^{-8}	4
$L_{A_{12}G}$	0.215	1.1×10^{-3}	2.366×10^{-7}	1.699×10^{-6}	2
$L_{A_{12}A_{13}}$	0.591	1.1×10^{-3}	2.366×10^{-7}	1.699×10^{-6}	5
$L_{A_6B_1}$	0.239	2.72×10^{-3}	2.62×10^{-6}	1.45×10^{-7}	2
$L_{B_1B_2}$	0.2	1.5×10^{-3}	2.8×10^{-9}	1.25×10^{-8}	2
$L_{B_2B_3}$	1.008	0.224×10^{-3}	5.55×10^{-7}	3.34×10^{-6}	10
$L_{A_9B_3}$	0.2	1.1×10^{-3}	1.699×10^{-7}	2.366×10^{-6}	2
$L_{A_5C_1}$	0.37	5×10^{-3}	2.8×10^{-9}	1.25×10^{-8}	4
$L_{C_1C_2}$	0.215	0.224×10^{-3}	5.55×10^{-7}	3.34×10^{-6}	2
$L_{A_8C_2}$	0.37	0.224×10^{-3}	5.55×10^{-7}	3.34×10^{-6}	4
$L_{D_1D_2}$	0.15	0.52×10^{-3}	4.3×10^{-7}	1.17×10^{-6}	2
$L_{D_2D_3}$	0.78	0.224×10^{-3}	5.55×10^{-7}	3.34×10^{-6}	5
L_{ID_3}=L_{JD_4}	0.15	0.224×10^{-3}	5.55×10^{-6}	3.34×10^{-7}	2
L_{IB_3}=L_{JA_9}	0.074	1.96×10^{-3}	3.12×10^{-9}	3.12×10^{-8}	2
$L_{D_3D_4}$	0.2	0.224×10^{-3}	5.55×10^{-7}	3.34×10^{-6}	10
$L_{D_4D_5}$	0.52	0.224×10^{-3}	5.55×10^{-7}	3.34×10^{-6}	2
$L_{D_5D_6}$	0.28	0.224×10^{-3}	5.55×10^{-7}	3.34×10^{-6}	4
$L_{D_6D_7}$=L_{A7H}	0.074	1.96×10^{-3}	3.12×10^{-9}	3.12×10^{-8}	2
$L_{D_8D_9}$	0.3	0.224×10^{-3}	3.34×10^{-7}	5.55×10^{-6}	2
$L_{D_9A_{13}}$	0.11	0.52×10^{-3}	1.17×10^{-7}	4.3×10^{-6}	4
L_{B_2H}	0.239	0.224×10^{-3}	5.55×10^{-9}	3.34×10^{-8}	4
L_{HB_3}	0.78	0.224×10^{-3}	5.55×10^{-7}	3.34×10^{-6}	10

notes: The first part of the table is the geometric parameters of configuration A. The first part plus the second part denote the geometric parameters of configuration B. The sum of parts 1, 2 and 3 is the geometric parameter of configuration C. The parameters of the entire table represent the geometric parameters of configuration D. When the parameters of configuration D are selected, $L_{B_1B_2}$ is replaced by the parameters of L_{B_2H} and L_{HB_3}.

TABLE 4. The mass of the drive motor.

Motor number	1-axis motor (θ_{i1})	2-axis motor (θ_{i2})	3-axis motor (θ_{i3})	4-axis motor (θ_{i4})
Mass of motor (kg)	14.4	11.5	14.4	3.8

by a large mass motor. The mass of the driving motor is very large, which will lead to the problem of a large amplitude of residual vibration at the end of the robot and a long attenuation time of the residual vibration. The branch chain described in this paper can move the motor at the driving joint of the series robot to or near the frame.

To avoid interference and singularity during the movement of the robot, the range of the driving angle of configuration A of the CM robot is $\theta_{A2} \in [-7.49, 37.40]$ and $\theta_{A3} \in [18.03, 70]$, respectively, in order to ensure that the motion spaces of configurations B, C and D remain unchanged after adding branch chains. According to equations (1)-(4), we can determine that the ranges of the driving angles of configurations B, C and D are $\theta_{B2} = \theta_{C2} = \theta_{D2} \in [-7.49, 37.40]$ and $\theta_{B3} = \theta_{C3} = \theta_{D3} \in [10.54, 107.40]$, respectively. Based on equation (6), we can calculate the moment of inertia

TABLE 5. Comparison of the moment of inertia of the CM robot.

Name	Axis	Maximum value of moment of inertia ($kg \cdot m^2$)	Minimum value of moment of inertia ($kg \cdot m^2$)	Mean value of moment of inertia ($kg \cdot m^2$)	Percentage reduction of maximum moment of inertia	Percentage reduction of minimum moment of inertia	Angles θ_{i2} (°) and θ_{i3} (°) corresponding to the maximum moment of inertia	Angles θ_{i2} (°) and θ_{i3} (°) corresponding to the minimum moment of inertia
A	X-axis	94.4186	64.2329	79.6836	—	—	(37.31°,18.03°)	(-7.49°, 69.93°)
	Z-axis	30.9700	19.0549	26.6135	—	—	(0.01°,18.13°)	(37.31°,69.93°)
B	X-axis	82.0661	65.2739	75.5339	13.08%	-1.62%	(37.31°,10.54°)	(3.51°,10.64°)
	Z-axis	25.7984	12.2860	20.5225	16.07%	35.52%	(-7.49°,107.34°)	(-7.39°,107.34°)
C	X-axis	81.7088	70.5332	77.2019	0.44%	-8.06%	(0.31°,10.54°)	(-7.49°,107.34°)
	Z-axis	27.1653	13.6269	21.6990	-5.03%	-10.91%	(3.21°,10.54°)	(-7.39°,107.34°)
D	X-axis	78.0117	72.8738	75.5930	4.52%	-3.32%	(-7.49°,34.54°)	(37.31°, 107.34°)
	Z-axis	18.6800	10.3849	14.9333	31.24%	23.79%	(2.41°,10.54°)	(37.31°,107.24°)

TABLE 6. Comparison of the residual vibration response of the CM robot configuration D.

Method of obtaining residual vibration response	Direction of residual vibration	Maximum amplitude(mm)	Error value(mm)
Simulation analysis	Y	0.496	0.098
	Z	1.370	-0.053
Theoretical calculation	Y	0.451	-0.104
	Z	1.198	-0.466
Experimental measurement	Y	0.553	—
	Z	1.664	—

FIGURE 12. Experimental test system for the residual vibration of the CM robot.

distribution of the entire workspace of four configurations, as shown in Figures 8-11.

Figure 8 shows that with an increasing driving angle θ_{A2} and driving angle θ_{A3}, the moment of inertia of configuration A of the CM robot about the x-axis gradually increases, and the variation range is [65 kg·m^2, 90 kg·m^2]. In addition, when the driving angle θ_{A2} and the drive angle θ_{A3} decrease gradually, the moment of inertia of configuration A

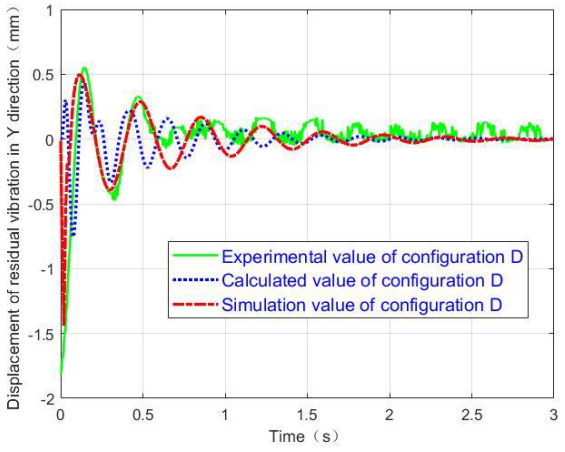

(a) Y direction

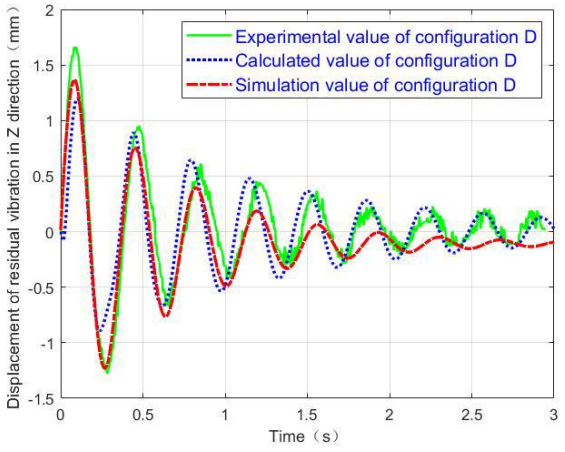

(b) Z direction

FIGURE 13. Comparison of the residual vibration response of the end point in configuration D with three branched chains.

about the z-axis increases, with a variation range of [20 kg· m^2, 30 kg· m^2]. When the driving angles θ_{A2} and θ_{A3} of the CM robot gradually decrease, the end effector of the robot gradually reaches the farthest position of the workspace. Therefore, it can be seen that the change in the moment of inertia is consistent with reality.

Figure 9 shows that with an increasing driving angle θ_{B2} and driving angle θ_{B3}, the moment of inertia of configuration B of the CM robot about the x-axis gradually increases, and the variation range is [66 kg· m^2, 82 kg· m^2]. When the driving angles θ_{B2} and θ_{B3} decrease gradually, the moment of inertia of configuration B about the z-axis increases gradually, and the variation range is [14 kg·m^2, 24 kg· m^2]. Comparing Figures 8 and 9, it can be seen that due to the addition of branch chain B_i, the forearm drive motor originally in the A_4 position is moved to joint B_2, which significantly reduces the moment of inertia of the entire robot about the x-axis and z-axis.

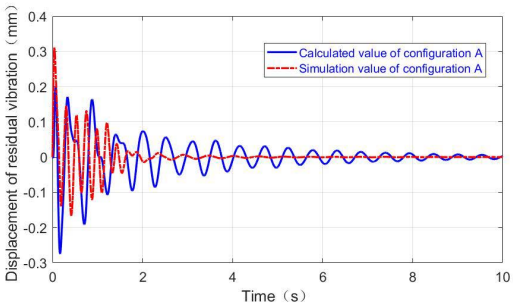

(a) Y direction

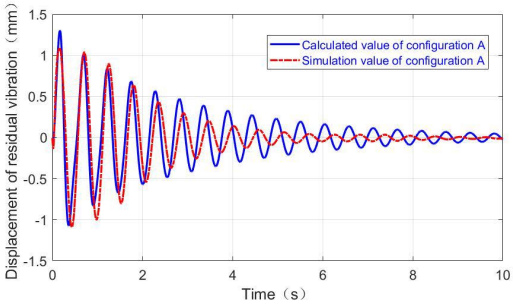

(b) Z direction

FIGURE 14. Comparison of the residual vibration response of configuration A without branched chain.

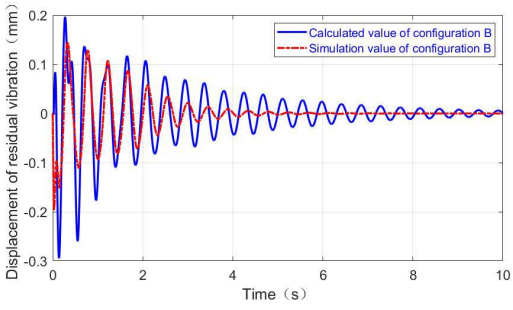

(a) Y direction

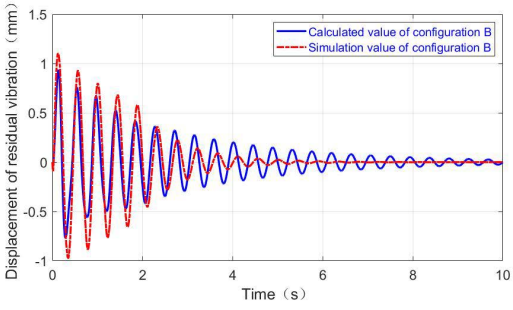

(b) Z direction

FIGURE 15. Comparison of the residual vibration response of configuration B with one branched chain.

According to Figure 10, with an increase in the driving angle θ_{C2}, the change in the moment of inertia of configuration C of the CM robot with respect to the x-axis is

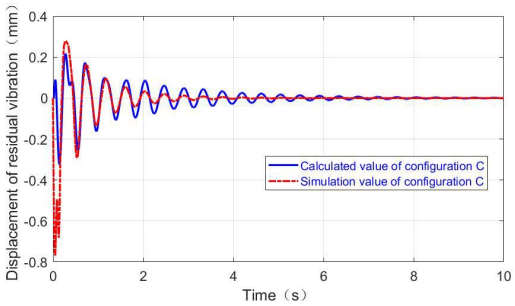

(a) Y direction

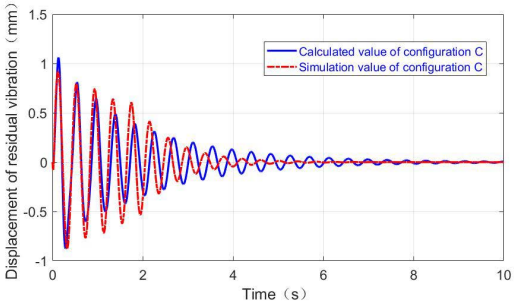

(b) Z direction

FIGURE 16. Comparison of the residual vibration response of configuration C with two branched chains.

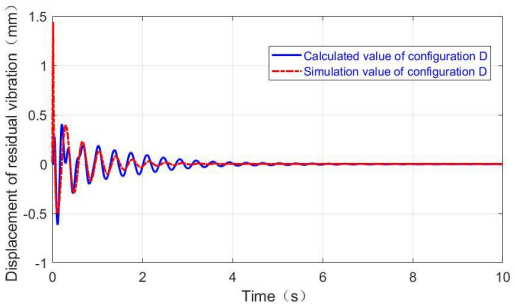

(a) Y direction

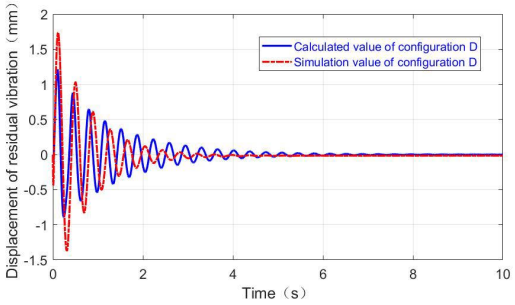

(b) Z direction

FIGURE 17. Comparison of the residual vibration response of configuration D with three branched chains.

small. With a decrease in the driving angle θ_{B3}, the change in the moment of inertia of configuration C about the x-axis increases gradually, and the variation range is [71 kg· m^2, 81 kg·m^2]. When the driving angles θ_{B2} and θ_{B3} decrease gradually, the moment of inertia of configuration C about the z-axis increases gradually, and the variation range is [8 kg·m^2, 26 kg·m^2]. When the driving angle θ_{C2} is the largest and the driving angle θ_{C3} is the smallest, the moment of inertia of configuration C about the z-axis reaches its maximum. Comparing Figure 9 and 10, it can be seen that due to the addition of the branch chain C_i, the driving motor originally in the A_2 position is moved to the joint C_1, and the variation range of the moment of inertia of the CM robot about the x-axis is reduced.

It can be seen from Figure 11 that with a decrease in driving angles θ_{D2} and θ_{D3}, the moment of inertia of configuration D of the CM robot about the x-axis gradually increases, and the variation range is [73kg·m^2, 78kg·m^2]. When the driving angles θ_{D2} and θ_{D3} decrease gradually, the moment of inertia of configuration C about the z-axis increases gradually, and the variation range is [11 kg·m^2, 18 kg·m^2]. Comparing Figure 10 and 11, it can be seen that due to the addition of the branch chain D_i, the driving motor originally in the A_{13} position is moved to the joint D_1, which reduces the variation range of the moment of inertia of configuration D.

From the above analysis, it can be seen that due to the hierarchical relationship of the branch chains, the driving motor away from the frame is installed near the frame, which significantly reduces the moment of inertia of the CM robot. According to Table 4, the maximum value and average value of the moment of inertia about the z-axis of the CM robot are significantly reduced. After the addition of the three branch chains, the average value of the x-axis moment of inertia of configuration D decreases by 5.13%, the maximum value decreases by 21.03%, and the minimum value increases by 13.45%. The mean value, maximum value, and minimum value of the moment of inertia of configuration D about the Z axis decreased by 43.89%, 39.68% and 45.5%, respectively.

According to Table 5, after adding branch chains in layers, the maximum and average moment of inertia of the CM robot in the Z direction are significantly reduced, while the moment of inertia in the X direction changes little. Because the rotation around the X axis is the expansion and contraction of the robot in the Z direction, the rotation around the Z axis is the rotation of the entire CM robot. Therefore, the moment of inertia in the Z direction is the largest factor affecting the residual vibration response.

VI. NUMERICAL SIMULATION AND EXPERIMENTAL STUDY

The dynamic simulation analysis of the CM robot virtual prototype shown in Figure 3 can obtain more reliable and relatively accurate residual vibration response results. The methods of simulation analysis and experimental research are as follows: First, the displacement response of the residual vibration at the D-end of the configuration is measured using high-speed photography. The measured results are filtered, and more accurate experimental results are obtained.

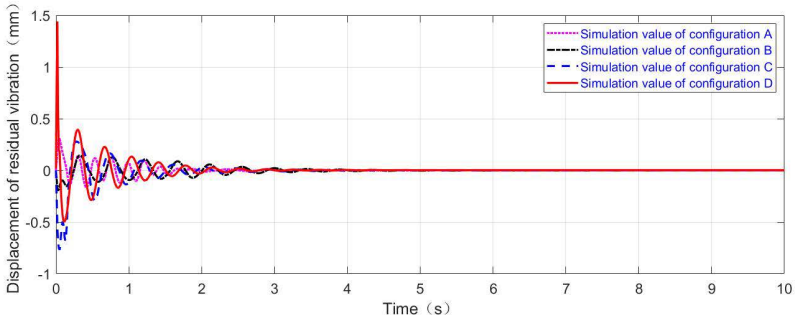

(a) Y direction

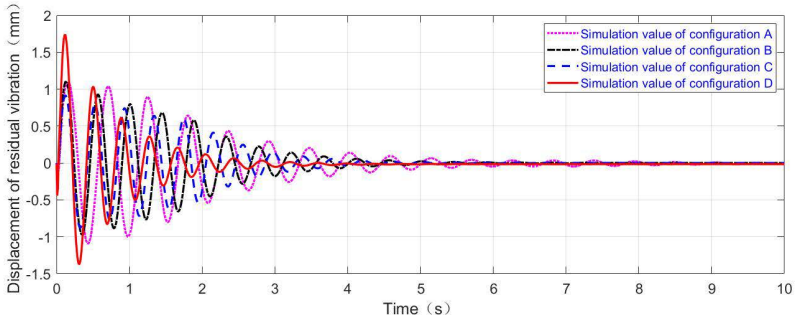

(b) Z direction

FIGURE 18. Comparison of the simulation analysis results of the residual vibration response of the CM robot.

Second, according to the experimental results, the dynamic model of configuration D is fitted using the Monte Carlo method to calculate the residual vibration displacement response of configuration D. Third, in the virtual simulation model of configuration D, the same constraints and boundary loads are set for the simulation. Then, the simulation results, calculation results and experimental results are compared to verify the correctness of the configuration D calculation model. The same constraints and boundary loads as configuration D are added to the virtual prototype models of configurations A, B and C. The displacement response of the residual vibration is then obtained via simulation analysis. According to the simulation results, the theoretical models of configurations A, B and C are fitted by the Monte Carlo method to solve the residual vibration displacement response. Finally, the correctness of the theoretical model is verified.

A. INTRODUCTION TO THE EXPERIMENTAL PLATFORM

As shown in Figure 12, the CM robot experimental test system is composed of the physical prototype of configuration D, the robot control system, a high-speed photography system, and computer and laser calibration. The component material of the CM robot prototype is 6061 aluminum alloy, and the joint bearing material is bearing steel.

In the experimental scheme, the high-speed photography is fixed, and the shooting position of the camera lens is the target position. The end of the robot is controlled to be far away from the target position, and the motor drives the robot to stop moving after the end reaches the target position. The residual vibration response at the end of the CM robot began to be measured via high-speed photography. The coordinates of the red points in all high-speed photographs are extracted to obtain the residual vibration responses in the Y and Z directions. In addition, it is worth noting that the movement of the CM robot is mainly in the YOZ plane. When the base rotates, the spatial configuration of the mechanism will not be changed. Therefore, the amplitude and period in the Y direction and Z direction are important indexes for analyzing the CM robot in this paper.

B. RESIDUAL VIBRATION RESPONSE ANALYSIS OF THE END OF CM ROBOT CONFIGURATION D

According to the experimental results, the theoretical model of configuration D is fitted using the Monte Carlo method. The specific values of the fitting parameters are $f_{DI_y} = 0.009$, $f_{DI_z} = 0.008$, $f_{DA} = 2.2$ and $f_{DJ} = 0.017$. Then, the residual vibration displacement response of configuration D of the CM robot is obtained by equation (29). Finally, the simulation analysis results, theoretical model calculation results and experimental test results are shown in Figure 13. To more clearly discuss the residual vibration of configuration D with three branches, we extracted the key information of Figure 13, as shown in Table 6. Next, we combine Figure 13 and Table 6 to verify the correctness of the conclusion.

According to Figure 13, the amplitude of the residual vibration response at the end of configuration D of the CM robot in

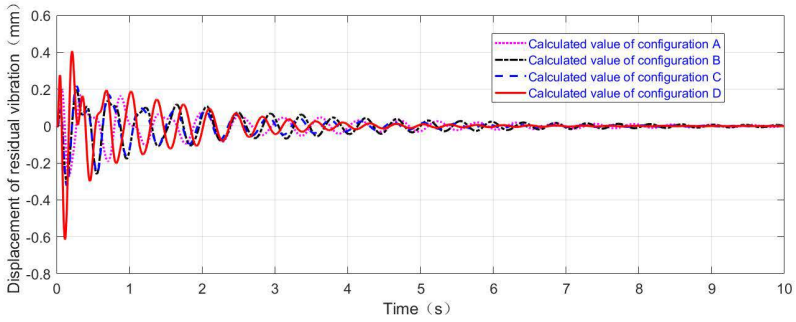

(a) Y direction

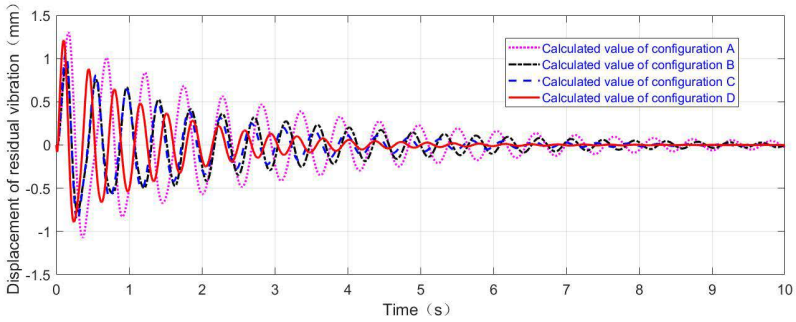

(b) Z direction

FIGURE 19. Comparison of the theoretical calculation results of the residual vibration response of the CM robot.

the Y direction is less than that in the Z direction. The amplitude and period of residual vibration from the simulation analysis, theoretical calculation and experimental results are essentially consistent. At the same time, the residual vibration in the Y direction has a large fluctuation at the beginning, which may be caused by other vibration types of the CM robot. This is also our next research direction.

According to Table 6, for the maximum amplitude in the Y direction, the simulation analysis result is 0.496 mm, the calculated value of the theoretical model is 0.451 mm, and the experimental measured value is 0.553 mm. The differences between the simulation analysis results, the theoretical calculation results and the experimental measured values are 0.045 mm and 0.057 mm, respectively. For the maximum amplitude in the Z direction, the simulation analysis result is 1.370 mm, the calculated value of the theoretical model is 1.198 mm, and the experimental measured value is 1.664 mm. The differences between the simulation analysis results, the theoretical calculation results and the experimental measured value are 0.294 mm and 0.466 mm, respectively. Therefore, the simulation analysis and theoretical model are verified.

C. COMPARATIVE ANALYSIS OF THE END RESIDUAL VIBRATION RESPONSE OF THE CM ROBOT

The virtual prototypes of configurations A, B and C of the CM robot are imported into Adams dynamic analysis software. The same constraint conditions and boundary loads of configuration D are applied to the virtual prototypes of configurations A, B and C, and the residual vibration response curves of each configuration end node A_{13} in the Y and Z directions are obtained.

According to the simulation results, the theoretical models of configurations A, B and C are fitted using the Monte Carlo method. The specific values of the fitting parameters are the same as configuration D. According to equation (29), the residual vibration response of each configuration of the CM robot can be obtained and compared with the simulation analysis results, as shown in Figures 14-17.

According to Figures 14-17, the residual vibration responses in the Y and Z directions at the end of each configuration of the CM robot are essentially consistent. The correctness of the simulation analysis model and theoretical calculation model has been verified.

As seen from Figures 18a and 19a, the amplitudes of residual vibration in the Y directions of each configuration of the CM robot are essentially the same, and the period and attenuation time of the residual vibration are suppressed. According to Figures 18b and 19b, the amplitude, period, and attenuation time of the residual vibration in the Z direction of configuration D of the CM robot are obviously suppressed. In the evolution from configuration A to configuration D, the residual vibration response of the CM robot is suppressed by adding different branch chains. The amplitude of the residual vibration of the CM robot decreases, and the attenuation time of the residual vibration becomes shorter, which improves the dynamic performance of the robot.

VII. CONCLUSION AND FUTURE WORK

A. CONCLUSION

In this paper, the current series robot was used as the host mechanism, and four configurations of the CM robot were obtained by optimizing the structural design of the robot. The CM robot combines the advantages of the CM mechanism and multi-DOF CM. By adding different branch chains, the moment of inertia of the CM robot is reduced. At the same time, the motor originally located at the joint can be reinstalled near the frame by adding different branch chains, which can suppress the residual vibration of the robot structurally.

The main contributions are as follows:

(1) The moment of inertia models of the four configurations of the CM robot are established and solved. The results show that the moment of inertia of the CM robot decreases with the addition of a branch chain. Specifically, after the four branch chains are added to configuration A, the maximum moment of inertia of the entire CM robot about the X axis is reduced by 21.03%, and the average value is reduced by 5.13%. The maximum value of the Z-axis moment of inertia decreases by 39.68% and the average value decreases by 43.89%.

(2) Based on the FEM and Timoshenko SBE model, the elastodynamic equations of the four configurations of CM robots are established, and the residual vibration responses of the four configurations of CM robots are solved using the Newmark method. The analysis of the residual vibration calculation results shows that the residual vibration of the CM robot can be suppressed by adding branch chains.

(3) The virtual prototype models of four configurations of the CM robot are established in ADAMS software, and the residual vibration response results are obtained via simulation analysis. The correctness of the theoretical models is verified by the simulation analysis.

(4) The residual vibration response of the end effector of configuration D is measured and compared with the theoretical model and simulation analysis. The results show that the theoretical model and simulation analysis are correct.

B. FUTURE WORK

In this paper, only the residual vibration of the CM robot was studied in detail. However, the nonlinear vibration problems in the process of CM robot motion, such as superharmonic resonance, subharmonic resonance, and combined resonance, need further theoretical analysis and experimental research. In addition, the experimental research on the residual vibration of CM robot needs to be improved, which is also a future direction for this research.

APPENDIX

NOMENCLATURE

The following symbols are used in this paper:

A_i, B_i, C_i, D_i	Kinematic pair number, $i = 1, 2, \ldots, 13$.
φ_i	Angle between link and horizontal direction, $i = 1, 2, \ldots, 7$.
θ_{ij}	The driving angle of the jth motor of configuration i, where $i = A, B, C, D, j = 1, 2, 3, 4$.
L_{ij}	Link length, i and j are kinematic pair numbers.
J_i	Moment of inertia about the i-Axis, $i = x, y, z$.
N	Link numbers.
m_i	The mass of link i, where i represents the link name.
m_j	jth motor mass, $j = \theta_1, \theta_2, \theta_3, \theta_4$
F_i	Fitting parameters, $i = y, z, I$.
a_c, b_c	Damping coefficient.
e_f	Generalized coordinate vector of Timoshenko SBE.
u_i	The displacement of node i along the x-axis of the local coordinate system.
v_i	The displacement of node i along the y-axis of the local coordinate system.
w_i	The displacement of node i along the z-axis of the local coordinate system.
θ_{xi}	The rotation angle of node i around the x-axis of the local coordinate system.
θ_{yi}	The rotation angle of node i around the y-axis of the local coordinate system.
θ_{zi}	The rotation angle of node i around the z-axis of the local coordinate system.
w_i	The elastic displacement along the x-axis after deformation of Timoshenko SBE, $i = x, y, z$.
$\phi\ (\bar{x}_P)$	Shape function of Timoshenko SBE.
E	The elastic modulus of Timoshenko SBE.
G	The shear modulus of Timoshenko SBE.
v	The Poisson's ratio of Timoshenko SBE.
σ_i	The normal stress component of Timoshenko SBE, $i = x, y, z$.
τ_i	The shear stress component of Timoshenko SBE, $i = xy, yz, zx$.
ε_i	The positive strain component of Timoshenko SBE, $i = x, y, z$.
γ_i	The shear strain component of Timoshenko SBE, $i = xy, yz, zx$.
U	The strain energy of Timoshenko SBE.
T	The kinetic energy of Timoshenko SBE.
b	The width of Timoshenko SBE.
h	The height of Timoshenko SBE.
l	The length of Timoshenko SBE.
I_i	The area moment of inertia of the Timoshenko SBE to the x-axis, $i = y, z$.
J	The polar moment of inertia of the Timoshenko SBE.
A	The cross-sectional area of Timoshenko SBE.
k	The correction factor of Timoshenko SBE.
K^e	The stiffness matrix of Timoshenko SBE.
M^e	The mass matrix of Timoshenko SBE.
C^e	The damping matrix of Timoshenko SBE.

R The transformation matrix between the local coordinate system and the system coordinate system.
ρ The material density of Timoshenko SBE.
F The generalized force array of applied load.
Q The force array applied by other units.
M_i The ith configuration mass matrix, $i = A, B, C, D$.
K_i The ith configuration stiffness matrix, $i = A, B, C, D$.
C_i The ith configuration damping matrix, $i = A, B, C, D$.
F_i The ith configuration external load force vector array, $i = A, B, C, D$.
Q_i The ith configuration inertial force array, $i = A, B, C, D$.
N_{ui} The ith configuration total number of system units, $i = A, B, C, D$.

ACKNOWLEDGMENT

The authors would like to thank the anonymous reviewers for providing critical comments and suggestions that improved the manuscript. Junjie Gong would like to thank Haifei Yang, School of public policy and management, Guangxi University, for her help in Academic English expression and writing.

REFERENCES

[1] M. H. Korayem, S. F. Dehkordi, and O. Mehrjooee, "Nonlinear analysis of open-chain flexible manipulator with time-dependent structure," *Adv. Space Res.*, vol. 69, no. 2, pp. 1027–1049, Jan. 2022.
[2] A. Ariano, V. Perna, A. Senatore, R. Scatigno, F. Nicolò, F. Fazioli, G. Avallone, S. Pesce, and A. Gagliano, "Simulation and experimental validation of novel trajectory planning strategy to reduce vibrations and improve productivity of robotic manipulator," *Electronics*, vol. 9, no. 4, p. 581, Mar. 2020.
[3] M. Aghajari, S. F. Dehkordi, and M. H. Korayem, "Nonlinear dynamic analysis of the extended telescopic joints manipulator with flexible links," *Arabian J. Sci. Eng.*, vol. 46, no. 8, pp. 7909–7928, Aug. 2021.
[4] L. Malgaca, Ş. Yavuz, M. Akdağ, and H. Karagülle, "Residual vibration control of a single-link flexible curved manipulator," *Simul. Model. Pract. Theory*, vol. 67, pp. 155–170, Sep. 2016.
[5] O. A. Garcia-Perez, G. Silva-Navarro, and J. F. Peza-Solis, "Flexible-link robots with combined trajectory tracking and vibration control," *Appl. Math. Model.*, vol. 70, pp. 285–298, Jun. 2019.
[6] S. Pellegrinelli, N. Pedrocchi, L. M. Tosatti, A. Fischer, and T. Tolio, "Multi-robot spot-welding cells for car-body assembly: Design and motion planning," *Robot. Comput.-Integr. Manuf.*, vol. 44, pp. 97–116, Apr. 2017.
[7] C. Deniz and M. Cakir, "In-line stereo-camera assisted robotic spot welding quality control system," *Ind. Robot: Int. J.*, vol. 45, no. 1, pp. 54–63, Jan. 2018.
[8] L. Banjanovic-Mehmedovic, F. Mehmedovic, I. Bosankic, and S. Karic, "Genetic re-planning strategy of wormhole model using neural learned vibration behavior in robotic assembly," *Automatika*, vol. 54, no. 4, pp. 483–494, Jan. 2013.
[9] N. Luan, H. Zhang, and S. Tong, "Optimum motion control of palletizing robots based on iterative learning," *Ind. Robot, Int. J.*, vol. 39, no. 2, pp. 162–168, 2012.
[10] B. Baksys, J. Baskutiene, and S. Baskutis, "The vibratory alignment of the parts in robotic assembly," *Ind. Robot: Int. J.*, vol. 44, no. 6, pp. 720–729, Oct. 2017.
[11] C. T. Kiang, A. Spowage, and C. K. Yoong, "Review of control and sensor system of flexible manipulator," *J. Intell. Robot. Syst.*, vol. 77, no. 1, pp. 187–213, 2005.
[12] Ş. Yavuz, L. Malgaca, and H. Karagülle, "Vibration control of a single-link flexible composite manipulator," *Composite Struct.*, vol. 140, pp. 684–691, Apr. 2016.
[13] S. H. Kim, E. Nam, T. I. Ha, S.-H. Hwang, J. H. Lee, S.-H. Park, and B.-K. Min, "Robotic machining: A review of recent progress," *Int. J. Precis. Eng. Manuf.*, vol. 20, no. 9, pp. 1629–1642, Sep. 2019.
[14] K. Lochan, B. K. Roy, and B. Subudhi, "A review on two-link flexible manipulators," *Annu. Rev. Control*, vol. 42, pp. 346–367, 2016.
[15] B. S. Thompson and C. K. Sung, "A variational formulation for the dynamic viscoelastic finite element analysis of robotic manipulators constructed from composite materials," *J. Mech. Design*, vol. 106, no. 2, p. 107, 1984.
[16] D. X. Liao, C. K. Sung, and B. S. Thompson, "The design of flexible robotic manipulators with optimal arm geometries fabricated from composite laminates with optimal material properties," *Int. J. Robot. Res.*, vol. 6, pp. 116–130, Sep. 1987.
[17] Ş. Yavuz, "An enhanced method to control the residual vibrations of a single-link flexible glass fabric reinforced epoxy-glass composite manipulator," *Compos. B, Eng.*, vol. 159, pp. 405–417, Feb. 2019.
[18] R. Bischoff, J. Kurth, G. Schreiber, R. Koeppe, A. Stemmer, A. Albu-Schäffer, O. Eiberger, A. Beyer, G. Grunwald, and G. Hirzinger, "Aus der forschung zum industrieprodukt: Die entwicklung Des.KUKA leichtbauroboters," *Automatisierungstechnik*, vol. 58, no. 12, pp. 670–680, Dec. 2010.
[19] U. Hagn, M. Nickl, S. Jrg, G. Passig, and G. Hirzinger, "The DLR MIRO: A versatile lightweight robot for surgical applications," *Ind. Robot., Int. J.*, vol. 35, no. 4, pp. 324–336, 2008.
[20] H. N. Rahimi and M. Nazemizadeh, "Dynamic analysis and intelligent control techniques for flexible manipulators: A review," *Adv. Robot.*, vol. 28, no. 2, pp. 63–76, 2014.
[21] J. Henikl, W. Kemmetmüller, T. Meurer, and A. Kugi, "Infinite-dimensional decentralized damping control of large-scale manipulators with hydraulic actuation," *Automatica*, vol. 63, pp. 101–115, Jan. 2016.
[22] H. Biglari, M. Golmohammadi, S. Hayati, and S. Hemmati, "Vibration reduction of a flexible robot link using a frictional damper," *J. Vibrat. Control*, vol. 27, nos. 9–10, pp. 985–997, May 2021.
[23] K. Kraus, Z. Šika, P. Beneš, J. Krivošej, and T. Vyhlídal, "Mechatronic robot arm with active vibration absorbers," *J. Vibrat. Control*, vol. 26, nos. 13–14, pp. 1145–1156, Jul. 2020.
[24] D. Subedi, I. Tyapin, and G. Hovland, "Review on modeling and control of flexible link manipulators," *Model., Identificat. Control, A Norwegian Res. Bull.*, vol. 41, no. 3, pp. 141–163, 2020.
[25] Y.-L. Wei, B. Li, P.-F. Ou, and Q.-Z. Zhang, "Hybrid input shaping control scheme for reducing vibration of robot based on multi-mode control," *J. Central South Univ.*, vol. 26, no. 6, pp. 1649–1660, Jun. 2019.
[26] T. Zhang, K. Lin, and A. Zhang, "Research on flexible dynamics of a 6-DOF industrial robot and residual vibration control with a pre-adaptive input shaper," *J. Mech. Sci. Technol.*, vol. 33, no. 4, pp. 1857–1889, 2019.
[27] J. Park and P.-H. Chang, "Learning input shaping technique for non-LTI systems," *J. Dyn. Syst., Meas., Control*, vol. 123, no. 2, pp. 288–293, Jun. 2001.
[28] S. Kapucu, G. Alici, and S. Bayseç, "Residual swing/vibration reduction using a hybrid input shaping method," *Mechanism Mach. Theory*, vol. 36, no. 3, pp. 311–326, Mar. 2001.
[29] C. Conker, H. Yavuz, and H. H. Bilgic, "A review of command shaping techniques for elimination of residual vibrations in flexible-joint manipulators," *J. Vibroeng.*, vol. 18, no. 5, pp. 2947–2958, Aug. 2016.
[30] D. Lee and C. W. Ha, "Optimization process for polynomial motion profiles to achieve fast movement with low vibration," *IEEE Trans. Control Syst. Technol.*, vol. 28, no. 99, pp. 1–10, Jun. 2020.
[31] B. Cao, T. Li, K. Sun, Y. Gu, M. Jin, and H. Liu, "Trajectory modified in joint space for vibration suppression of manipulator," *IEEE Access*, vol. 6, pp. 57969–57980, 2018.
[32] W. He, T. Wang, X. He, L. Yang, and O. Kaynak, "Dynamical modeling and boundary vibration control of a rigid-flexible wing system," *IEEE/ASME Trans. Mechatronics*, vol. 25, no. 6, pp. 2711–2721, Dec. 2020.
[33] Z. Jianying, L. Tun, and Z. Zhiping, "Study on component synthesis active vibration suppression method using zero-placement technique," *Chin. J. Aeronaut.*, vol. 21, no. 4, pp. 304–312, Aug. 2008.
[34] D. K. Thomsen, R. Søe-Knudsen, O. Balling, and X. Zhang, "Vibration control of industrial robot arms by multi-mode time-varying input shaping," *Mech. Mach. Theory*, vol. 155, Jan. 2021, Art. no. 104072.
[35] H. J. Yoon, S. Y. Chung, H. S. Kang, and M. J. Hwang, "Trapezoidal motion profile to suppress residual vibration of flexible object moved by robot," *Electronics*, vol. 8, no. 1, p. 30, Jan. 2019.

[36] Z.-C. Qiu, J. Yang, and X.-M. Zhang, "Self-excited vibration control of the flexible planar parallel 3-RRR robot," *J. Vibrat. Control*, vol. 25, no. 2, pp. 351–361, Jan. 2019.
[37] L. Sun, W. Yin, M. Wang, and J. Liu, "Position control for flexible joint robot based on online gravity compensation with vibration suppression," *IEEE Trans. Ind. Electron.*, vol. 65, no. 6, pp. 4840–4848, Jun. 2018.
[38] S. S. Ge, T. H. Lee, J. Q. Gong, and Z. P. Wang, "Model-free controller design for a single-link flexible smart materials robot," *Int. J. Control*, vol. 73, no. 6, pp. 531–544, Jan. 2000.
[39] W. S. Jang, K. S. Kim, and S. K. Lee, "An open-loop control scheme for minimization of residual vibrations of a flexible robot," *Experim. Mech.*, vol. 43, no. 4, pp. 387–395, Dec. 2003.
[40] M. Sayahkarajy, Z. Mohamed, and A. A. Mohd, "Review of modelling and control of flexible-link manipulators," *Proc. Inst. Mech. Eng., I, J. Syst. Control Eng.*, vol. 230, pp. 861–873, Sep. 2016.
[41] Q. Zhang, Q. Lu, X. Zhang, and J. Wu, "Study on residual vibration suppress of a 3-DOF flexible parallel robot mechanism," *Sensors*, vol. 18, no. 12, p. 4145, Nov. 2018.
[42] K. Bai, M. Luo, T. Li, J. Wu, L. Yang, M. Liu, and G. Jiang, "Active vibration adaptive fuzzy backstepping control of a 7-DOF dual-arm of humanoid robot with input saturation," *J. Intell. Fuzzy Syst.*, vol. 31, no. 6, pp. 2949–2957, Dec. 2016.
[43] M. A. Hosseini and H. M. Daniali, "Cartesian workspace optimization of tricept parallel manipulator with machining application," *Robotica*, vol. 33, no. 9, pp. 1948–1957, Nov. 2015.
[44] J. Gong, W. Wei, G. Cai, Y. Liu, and S. Peng, "Kinematic performance analysis of a controllable mechanism welding robot with joint clearance," in *Proc. MATEC Web Conf.*, vol. 327, 2020, p. 03006.
[45] W. Wei, G. Cai, J. Gong, and C. Ban, "A host-parasite structural analysis of industrial robots," *Int. J. Adv. Robot. Syst.*, vol. 17, no. 5, pp. 1–17, 2020.
[46] W. Wei, G. Cai, J. Gong, and S. Peng, "Modeling and analysis of the stiffness distribution of Host–Parasite robots," *IEEE Access*, vol. 9, pp. 86300–86320, 2021.
[47] G. Chen, X. Zeng, X. Liu, and X. Rui, "Transfer matrix method for the free and forced vibration analyses of multi-step Timoshenko beams coupled with rigid bodies on springs," *Appl. Math. Model.*, vol. 87, pp. 152–170, Nov. 2020.

JUNJIE GONG was born in 1995. He received the B.S. degree in mechanical manufacturing and its automation from Wuhan Polytechnic University, Wuhan, China, in 2018. He is currently pursuing the Ph.D. degree with Guangxi University, China. His research interests include mechanical innovation design, industrial robots, nonlinear vibrations theory, nonlinear systems control, and mechanical dynamics.

GANWEI CAI was born in 1961. He received the Ph.D. degree from the Huazhong University of Science and Technology, China, in 1998. He was a Postdoctoral Researcher at Central South University, China, in 1998. From 2009 to 2010, he joined Professor Jiansheng Dai as a Visiting Scholar at the Centre for Robotics Research, King College London, University of London, London, U.K. He is currently a Professor with the School of Construction Machinery, Hunan Sany Polytechnic College. He is the author of three books, more than 180 articles, and more than 170 inventions. His research interests include the theory of mechanisms and machines, mechanical dynamics, and nonlinear vibration theory.

WEI WEI was born in 1984. He received the Ph.D. degree from the South China University of Technology, China, in 2021. He is currently working with Guangxi University, Nanning, China. His research interests include bionic robot design, host–parasite mechanisms, and spatial multiloop coupling mechanisms.

KECHEN ZHANG was born in 1994. He received the B.S. degree in mechanical manufacturing and its automation from the Changchun Institute of Technology, Changchun, China, in 2017. He is currently pursuing the M.S. degree with Guangxi University, China. His research interests include industrial robots, nonlinear vibrations, and mechanical dynamics.

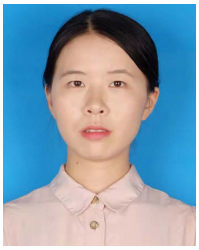

SIXU PENG was born in 1995. She received the B.S. degree from Shenyang Ligong University, China, in 2017. She is currently pursuing the M.S. degree with Guangxi University, China. Her research interests include robotic mechanisms, mechanical dynamics, and nonlinear vibrations.